Quantifying Phase Transformations in Alloying Anodes via *in-situ* Liquid Cell Hard X-ray Spectroscopy and Cryogenic Microscopy

Neil Mulcahy,[1] Syeda Ramin Jannat,[1] Yaqi Li,[1] Tigran Simonian,[1] Mariana Palos,[1] James O. Douglas,[1] Jessica M. Walker,[2] Baptiste Gault,[1,3,4] Mary P. Ryan,[1] and Michele Shelly Conroy[1,*]

[1]*Department of Materials and London Centre for Nanotechnology, Imperial College London, Exhibition Road, London SW7 2AZ, United Kingdom*

[2]*Diamond Light Source, Harwell Science and Innovation Campus, Didcot, United Kingdom*

[3]*Max-Planck Institute for Sustainable Materials, Max-Planck Straße 1, 40237, Düsseldorf, Germany*

[4]*Université de Rouen Normandie, CNRS, INSA Rouen Normandie, Groupe de Physique des Matériaux, UMR 6634, F-76000 Rouen, France*

(Received 4 December 2025; revised 8 April 2026; accepted 9 June 2026; published 12 August 2026)

Understanding electrochemical phenomena at complex liquid-solid interfaces requires linking real-time structural dynamics with atomic-scale interfacial chemistry. Here, we integrate *in-situ* synchrotron X-ray fluorescence and diffraction with high-resolution cryogenic electron and ion multimodal microscopy to provide a mechanistic understanding of Pt-based alloying anodes across length scales. We directly observe the initial lithiation-driven formation of Li_2Pt and its evolution to a stable LiPt intermetallic phase during extended cycling via a solid-solution type reaction mechanism. Simultaneously, the solid-electrolyte interphase transitions from an unstable carbonate-rich to a stable LiF-dominated composition, confirmed by cryogenic scanning transmission electron microscopy-electron energy loss spectroscopy. Crucially, cryogenic atom probe tomography reveals spatially distinct compositional regimes within the alloy anode: a lithium-flux-limited, heterogeneous interfacial zone and a diffusion-controlled, homogeneous LiPt alloy bulk. This nanoscale compositional gradient rationalizes the emergent solid-solution reaction mechanism and highlights how kinetic limitations and interface dynamics govern alloy formation and electrochemical stability. Our findings establish a correlative experimental framework that directly links *in-situ* structural dynamics with preserved near-atomic resolution interfacial chemistry, advancing the rational design of durable alloy electrodes for next-generation energy storage.

DOI: 10.1103/r3tc-hr17

I. INTRODUCTION

The performance and stability of electrochemical energy storage devices are governed by dynamic processes at liquid-solid interfaces [1–3]. Here, the transport of ions and electrons drives phase transformations, the evolution of interphases, and ultimately degradation [4–6]. Capturing these phenomena with high spatial and chemical resolution remains a significant challenge, as many are highly transient, atomic-scale processes [7–9] that are sensitive to environmental exposure and susceptible to irradiation damage, particularly from electron beams [10–12].

Operando liquid-based platforms, such as liquid cell transmission electron microscopy (LCTEM), have enabled direct observation of battery processes at high temporal and spatial resolutions [8,13,14] while maintaining systems in their native environment. However, the presence of liquid in the cell increases incident beam scattering, fundamentally limiting the ability to acquire detailed spectroscopic information or to identify interphase compositions and electrode crystalline phases [15–17]. In the case of LCTEM, electron beam irradiation can induce various damage mechanisms such as radiolysis, further restricting critical analysis [12,16].

Synchrotron-based hard X-ray nanoprobe techniques, including X-ray fluorescence (XRF) mapping and X-ray diffraction (XRD), provide powerful *in-situ* tools for probing the chemistry and structure of electrochemical systems in liquid environments [18–21]. In contrast to electron microscopy, these techniques can probe larger liquid volumes and electrode materials with minimal scattering and reduced beam damage [19,22]. Currently, relatively few studies have applied hard X-ray nanoprobes to anode-electrolyte interfaces under realistic electrochemical conditions. However, recent developments in

*Contact author: m.conroy@imperial.ac.uk

confined liquid cell platforms incorporating nanoscale patterned electrodes and nanoprobe synchrotron optics have enabled nanoscale spatially resolved XRD and XRF measurements under operando conditions [18,23,24].

Despite these advances, important limitations remain in analyzing electrochemical interfaces. Light elements (e.g., H, Li, C, O, and F), which dominate SEI chemistry, exhibit weak scattering factors and low fluorescence yields in the hard X-ray regime. As a result, they are better probed using surface sensitive techniques like soft X-ray absorption spectroscopy (XAS). However, the shallow penetration depth and vacuum requirements of soft XAS make operando measurements in liquid electrolytes experimentally challenging [21,25]. Further, extended acquisition times required for nanoscale mapping over representative micron-scale electrode areas under liquid conditions can make it difficult to follow highly transient or spatially inhomogeneous reactions.

Addressing these challenges requires correlative approaches that integrate operando or *in-situ* measurements with high-resolution cryogenic microscopy. Methods such as cryogenic atom probe tomography (cryo-APT) and cryogenic scanning transmission electron microscopy (cryo-STEM) have emerged as powerful tools for probing electrochemical processes [9,26]. Previous studies have successfully correlated LCTEM observations with cryo-APT analysis, capturing transient electrochemical phenomena while preserving the final interphase layer and electrode composition at near-atomic scale resolutions [9,26]. These advances highlight the potential of cryogenic correlative techniques to bridge the gap between dynamic operando measurements and atomic-scale structural and compositional characterization.

Cryo-APT provides unparalleled near-atomic-scale compositional insight into preserved interfacial regions, particularly for light elements central to SEI chemistry [27,28]. Cryo-STEM, when combined with spectroscopy techniques such as electron energy loss spectroscopy (EELS) and energy dispersive X-ray (EDX) spectroscopy, offers high spatial and chemical resolution imaging of electrode morphology and local composition, enabling detailed mapping of interfacial regions and identification of nanoscale phases or SEI components [10,29,30]. By correlating these complementary measurements, it becomes possible to directly link structural transformations, elemental migration, and interfacial stability across multiple length scales, thereby providing mechanistic insights into alloying reactions, SEI evolution, and electrode reversibility in next-generation battery materials.

While operando hard X-ray nanoprobes and cryogenic microscopy have each independently advanced the study of electrochemical interfaces, their integration within a unified, multiscale correlative workflow for buried anode-electrolyte interfaces remains limited. In particular, dynamic nanoscale XRD and XRF measurements have rarely been directly linked to near-atomic scale compositional mapping of the resulting alloy phases and interphases. Establishing such a correlation is essential for connecting real-time structural evolution with preserved interfacial chemistry.

Here, we apply this combined methodology to a model Pt alloy anode. Pt offers a simplified system in which alloying and dealloying steps are well defined and readily tracked. By contrast, technologically relevant materials such as Si, Sn, and Al exhibit far greater complexity, with larger volume changes, heterogeneous SEI formation, and complex alloying pathways. By bridging operando structural insights with near-atomistic compositional mapping, our approach establishes a transferable correlative framework that can be extended to these more challenging chemistries, providing mechanistic foundations for the design of durable next-generation energy storage systems. In this context, the Pt model system functions as a benchmark, enabling method validation and providing foundational insights for the rational design of durable, high-performance energy storage systems.

II. MATERIALS AND METHODS

A. Synchrotron *in-situ* liquid cell setup

The *in-situ* liquid set up at the hard X-ray nanoprobe I14 beamline at Diamond Light Source (Didcot, UK) has been described in numerous reports [18,23,24,31]. For this work, the nanocell was composed of liquid cell electrochemical biasing nanochips which are commercially available from DENSsolutions B.V. (Delft, The Netherlands). Importantly, the commercial liquid cell electrochemical nanochips used here are the same as those widely employed in liquid cell TEM studies, enabling a direct comparison of the electrochemical and fluidic environments between the X-ray beamline and the TEM. The bottom chip contains a three-electrode setup involving a working, reference, and counter electrode made of Pt. The working electrode has a geometric surface area of $\approx 3.7 \times 10^{-5}$ cm^2 and is deposited on a 50 nm SiN_x electron transparent membrane window with dimensions of approximately 20 μm × 200 μm [32]. Combined with an identical SiN_x membrane window on the top nanochip, the electrodes of interest could be viewed.

While liquid flow is possible with this setup, it was avoided to mitigate any potential air contamination due to the air- and moisture-sensitive nature of the Li-based electrolyte used in this experiment [2,33,34], $LiPF_6$ in ethylene carbonate/dimethyl carbonate (EC/DMC), supplied by Merck Life Science UK Ltd (Dorset, United Kingdom). Instead, the nanocell with electrolyte was entirely constructed within an Ar glovebox, the LABmaster SP glovebox supplied by MBRAUN (Garching, Germany), and this process is illustrated in Fig. 1.

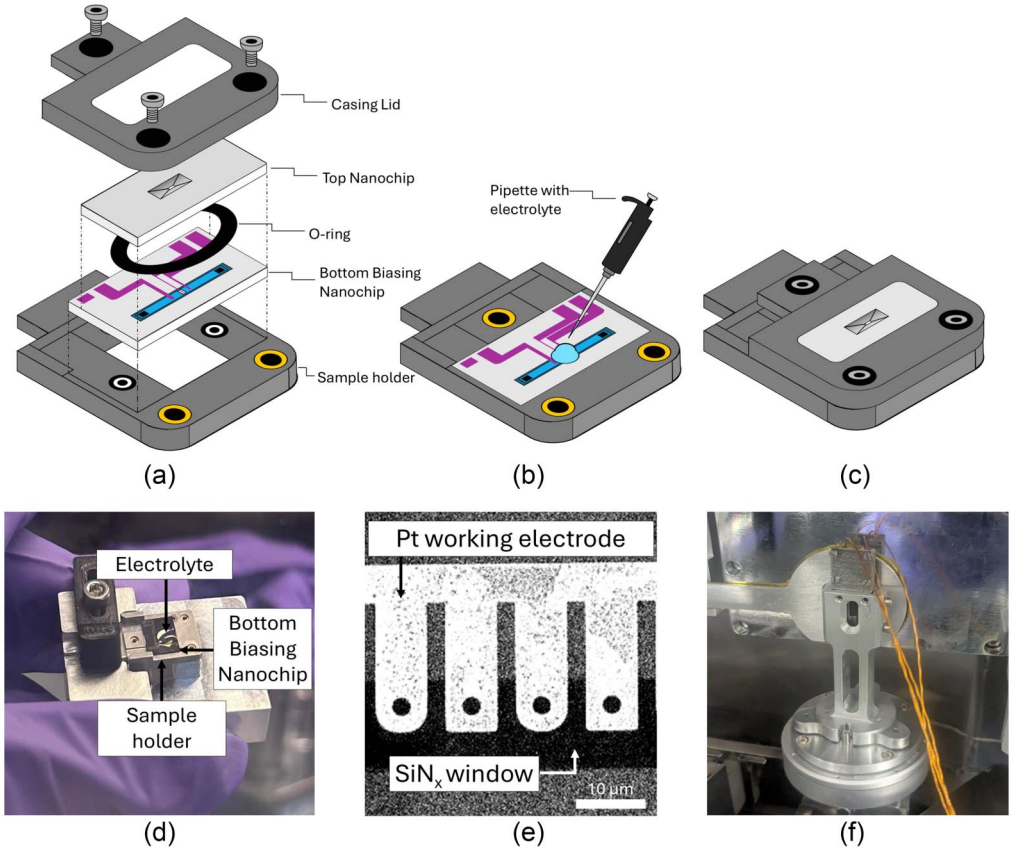

FIG. 1. Overview of the synchrotron *in-situ* nanocell preparation process. (a) Schematic of the contents of a fully assembled sample, comprising the sample holder, bottom biasing nanochip, EPDM O-ring, top nanochip, and casing lid. (b) Schematic illustrating drop-casting of the Li electrolyte onto the bottom biasing nanochip using a pipette within the Ar glovebox. (c) Schematic of the completed, sealed nanocell containing electrolyte. (d) Photograph showing an example of the electrolyte drop cast on the nanochip. (e) SEM image showing the geometry of the Pt working electrode. (f) Photograph of the assembled sample holder mounted on the beamline scanning stage and connected to a potentiostat.

The sample setup is composed of the top and bottom Si wafer nanochips, an ethylene propylene diene monomer (EPDM) O-ring, the sample holder and the casing lid. These elements are represented schematically in Fig. 1(a). The bottom nanochip containing the three Pt electrode set up was placed into the sample holder. A pipette was then used to drop cast ≈1 μl of electrolyte onto the bottom nanochip, as in Fig. 1(b). A photograph of this process can be seen in Fig. 1(d). The top nanochip with an O-ring was placed on top of the bottom nanochip before the two were sealed together by securely screwing the casing lid into the sample holder, as in Fig. 1(c). During this construction process, it was ensured that the inlet and outlet holes on the nanochip were completely sealed to prevent any air exposure during transport from the glovebox to the beamline and to avoid any electrolyte leakage. Due to challenges in assembling the nanocells within the glovebox, a window alignment check was performed outside.

Once the sample had been constructed, it was removed from the glovebox, and contact pads on the bottom nanochip were attached to external electrochemical contacts. This was subsequently connected to an external potentiostat, the SP-200 potentiostat, controlled via EC-Lab®, both supplied by BioLogic (Seyssinet-Pariset, France). Details on the biasing conditions for specific experiments will be given in their respective sections. A scanning electron microscopy (SEM) image showing an example of the shape of the working electrode is shown in Fig. 1(e). Once assembled, the sample is mounted on the beamline scanning stages using a holder on a kinematic mount, as described by Kerkhof *et al.* [18]. A photograph of the sample mount on the beamline scanning stage can be seen in Fig. 1(f).

B. X-ray diffraction and X-ray fluorescence

Samples were analyzed using a focused X-ray beam with a spot size of 50×50 nm. The beamline setup is such that simultaneous XRD and XRF data could be acquired. XRF measurements were acquired via continuous raster scanning using a four-element silicon drift detector supplied by RaySpec (High Wycombe, UK) positioned in a backscatter geometry. Simultaneously,

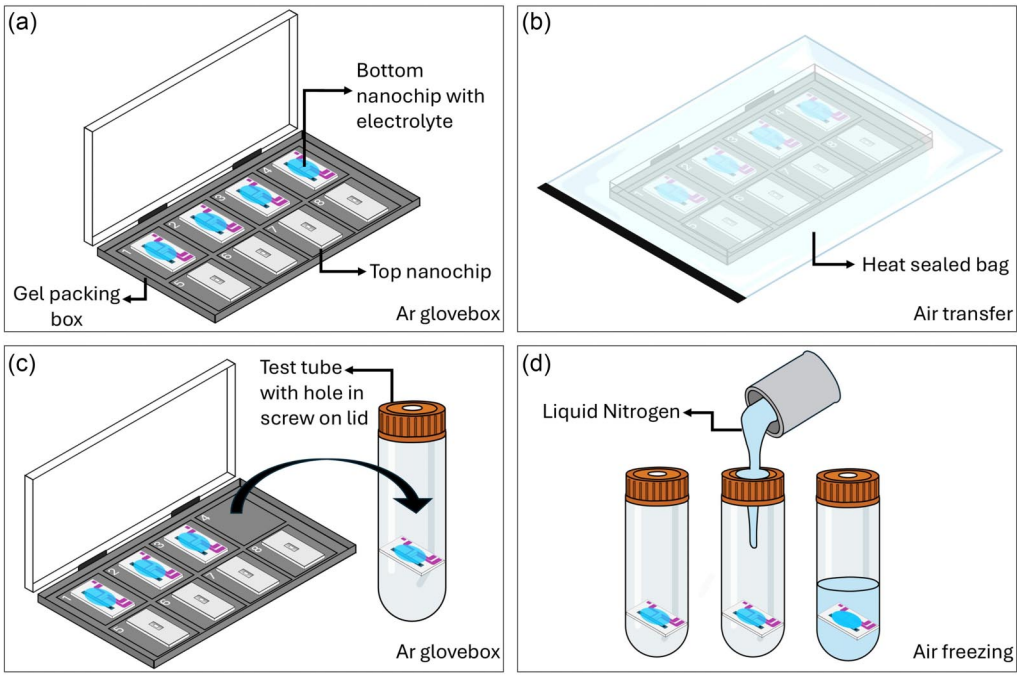

FIG. 2. Schematics illustrating the transfer and freezing process. (a) Bottom and top nanochips placed in a gel-packing box within an Ar glovebox at the synchrotron facility following X-ray experiments. (b) The gel box sealed with parafilm, heat-sealed in a bag, and removed from the glovebox for transfer in air. (c) Inside an Ar glovebox at the cryogenic facility at Imperial College London, the bottom nanochips, containing the liquid-solid interface, are placed into test tubes sealed with screw-on lids containing a small hole. (d) The test tubes are removed from the glovebox, and LN_2 is poured through the hole, freezing the nanochip and electrolyte.

XRD measurements were recorded in transmission geometry using the Excalibur detector supplied by Diamond Light Source (Didcot, UK). All XRD measurements were taken at 18 keV, covering a Q range of 0–4.8 $Å^{-1}$. Specific acquisition parameters such as exposure time, scan step size and scan area will be described within the relevant results sections. More information on the beamline setup is described by Quinn *et al.* [24].

To perform initial screening and quality assessment of the collected datasets, raw XRF and XRD datasets were first prescreened using DAWN (Data Analysis WorkbeNch), supplied by Diamond Light Source (Didcot, UK). Following prescreening, XRF datasets were extracted from processed synchrotron files in the NeXus (.nxs) format using custom Python code. Element-specific intensity maps (Pt-Lα) were normalized to the global maximum intensity and plotted as spatial distributions using the recorded X and Y scan coordinates. Resulting maps were visualized with a consistent color scale.

Raw XRD datasets were preprocessed using an asymmetric least squares (ALS) smoothing algorithm implemented in Python to subtract the background and isolate the true diffraction signal. Data below $Q = 1$ $Å^{-1}$ were excluded to minimize low-angle noise, and the resulting baseline-corrected datasets were saved in CSV format. These were subsequently imported into Origin plotting software for manual peak fitting, where peak positions, intensities, full width at half maximum (FWHM), and coefficients of determination (R^2) were recorded. To identify possible phases, the fitted peak positions were compared against a reference library of simulated diffraction patterns using a custom Python script. Candidate phases were assigned based on a ± 0.015 $Å^{-1}$ tolerance in q-space. All custom Python scripts used for data processing and analysis are provided as Jupyter notebooks in the Supplemental Material [35]. Brief descriptions of each notebook's functionality are also included.

C. Transfer and freezing process

After each *in-situ* X-ray experiment, the sample holder was removed from the beamline and transferred to the Ar glovebox. This transfer process would take approximately 5 min. The cell was immediately disassembled with minimal disturbance to the electrolyte, and the nanochips were placed in a gel-packing box to preserve the liquid-solid interface, as shown in Fig. 2(a).

The gel box was sealed with Parafilm, heat-sealed in a bag as in Fig. 2(b), and transferred from Diamond Light Source to an Ar glovebox at Imperial College London within 48 h. During transport, the sealed nanochips were enclosed in airtight, Ar-filled packaging and exposed only indirectly to ambient air for approximately 4 h. Within the Ar glovebox at Imperial College, each bottom nanochip was placed in a test tube, capped with a lid containing a

small hole, and removed from the glovebox. An example of this process is shown in Fig. 2(c). Liquid nitrogen (LN_2) was poured through the hole to freeze the nanochip and electrolyte, with the heavier Ar atmosphere minimizing air exposure, as in Fig. 2(d). The frozen nanochips could then be transferred to the cryo-stage of the PFIB/SEM for further analysis, as described by Mulcahy *et al*. [26].

D. Vacuum cryo transfer module and inert glovebox

A vacuum cryo transfer module (VCTM) from Ferrovac GmbH (Zürich, Switzerland) was used to transfer samples between instruments, maintaining them under vacuum/inert conditions and at constant cryogenic temperatures. This module features a compact ion pump and a non-evaporable getter cartridge, maintaining pressures down to 10^{-10} mbar. Cryogenic temperatures can be sustained within the module via an integrated dewar of LN_2. The module can accommodate standard and cryo-compatible sample pucks supplied by CAMECA Inc. (Madison, WI, USA). The system contains a 500 mm wobblestick with a PEEK-insulated puck manipulator allowing pucks to be picked up or released [36].

Cryogenic sample preparation was carried out in an inert nitrogen glovebox supplied by Sylatech Ltd (York, UK) and is operated with typical oxygen and humidity content below 5 ppm. LN_2 can be delivered directly into an internal bath via a pressurized external dewar, the Apollo 50 dewar supplied by Cryotherm GMBH (Kirchen (Sieg), Germany), enabling in-glovebox freezing. Samples can be transferred under cryogenic and vacuum conditions to a VCTM using a vertical transfer "elevator" which can be cooled in a similar manner. The elevator can be raised into a pumpable loadlock chamber, which is directly connected to a Ferroloader docking station (Ferrovac GMBH, Zürich, Switzerland), allowing samples to be pulled into the module via a PEEK-insulated puck manipulator, maintaining the sample under vacuum and at cryogenic temperatures.

E. Plasma focused ion beam/scanning electron microscope with cryogenic capabilities

All focused ion beam (FIB)/SEM work was carried out using a Thermo Fisher Scientific Helios Hydra CX (5CX) plasma FIB system (Waltham, MA, USA), equipped with an Easylift tungsten cryo-micromanipulator and an Aquilos cryo-stage. The cryo system operates via a closed-loop flow of gaseous nitrogen cooled through a heat exchanger immersed in an external LN_2 dewar. This setup enabled cooling of both the stage and micromanipulator to approximately 90 K. A steady nitrogen gas flow rate of 180 mg/s was maintained to reach and sustain this base temperature. The temperature of the system, including both the stage and micromanipulator, could be controlled using a cryogenic temperature controller, Model 335, supplied by LakeShore Cryotronics Inc. (Westerville, OH, USA), in conjunction with integrated stage heaters. The instrument also includes a Ferroloader docking station, Ferrovac GmbH (Zürich, Switzerland), which allows direct transfer of cryogenic specimens from a VCTM onto the cryo stage without heating up or direct exposure to the atmosphere.

For these experiments, a "dual-puck" stage baseplate supplied by Oxford Atomic (Oxford, UK) was employed, accommodating two standard cryopucks supplied by CAMECA Instruments Inc. (Madison, WI, USA) simultaneously. Typically, one puck would contain the frozen liquid cell nanochip, while the other would contain a preprepared Si microarray coupon for cryo-APT specimen preparation or a molybdenum TEM lift-out grid for cryogenic TEM lamella preparation. For cryo-APT, the Si microarray coupon was prepared first at room temperature, including precutting the posts at 0°, while also coating the posts in SEMGlu™, supplied by Kleindiek Nanotechnik GmbH (Reutlingen, Germany) [37]. This room-temperature preparation procedure is detailed by Mulcahy *et al.* [38]. The FIB column was aligned at 52° relative to the SEM column.

F. Cryogenic scanning transmission electron microscopy

The EleCryo double tilt vacuum-transfer holder (Mel-Build, Fukuoka, Japan) was used for all STEM measurements. This holder allowed prepared TEM samples to be transferred under vacuum or inert conditions and subsequently cooled to cryogenic temperatures within the TEM instrument. Cryogenically prepared lamellae were loaded into the holder inside the nitrogen glovebox, preventing any ambient exposure throughout the entire process.

A Thermo Fisher Scientific (Waltham, Massachusetts, United States) Spectra 300 (S)TEM at a 300 kV accelerating voltage was used for all STEM measurements. This instrument is probe-corrected and fitted with an ultrahigh-resolution X-FEG Ulti-monochromator, a Gatan Continuum energy filter and a K3 direct electron detector. Prior to any measurements, the holder was allowed to reach stable LN_2 temperatures (≈77 K) to minimize noise during acquisition. The measured screen current during STEM imaging was 17 pA with a probe converge angle of 30 mrad. EDX maps were acquired using a Dual-X energy EDX detector with a measured screen current of 11 pA, a dwell time of 1 μs per pixel and a pixel size of 2.77 nm, corresponding to an estimated electron dose of ∼9 e^- nm^{-2} per frame. Multiple frames were acquired and summed together to provide sufficient signal and improve signal-to-noise. Elemental maps were quantified in terms of weight percent (wt %) and processed using Velox supplied by Thermo-Fischer Scientific (Waltham, Massachusetts, United States).

4D-STEM datasets were acquired in nanobeam diffraction mode using a probe convergence semi-angle of 2.5 mrad over a 64×48 probe position grid with a step size of 4.2 nm. Diffraction patterns were recorded on a Gatan K3 direct electron detector with a camera length of 145 mm and were summed using Gatan Digital Micrograph 3.62 (Gatan Inc., Pleasanton, CA, USA) prior to further analysis.

STEM-EELS datasets were acquired in energy-filtered TEM (EFTEM) mode with a camera length of 145 mm. The convergence and collection semi-angles were 40.5 and 156.5 mrad, respectively. The energy dispersion was 0.03 eV/channel and the energy resolution, determined from the FWHM of the zero-loss peak, was 1 eV. For each area, 40 sequential frames were recorded, drift-corrected, and summed to improve the signal-to-noise ratio for subsequent data analysis in Gatan Digital Micrograph 3.62 (Gatan Inc., Pleasanton, California). Spectra were acquired with a pixel time of 0.002031s and a pixel size of 3 nm. Based on a probe current of ~17 pA, this corresponds to an estimated cumulative electron dose of approximately 2.4×10^4 $e^- nm^{-2}$ (~240 $e^- Å^{-2}$).

G. Cryogenic atom probe tomography

APT experiments were conducted using a Local Electrode Atom Probe 5000 XR (LEAP 5000 XR) instrument, manufactured by CAMECA Instruments Inc. (Madison, WI, USA). The system is equipped with a reflectron time-of-flight mass spectrometer and a Ferro-Loader docking station, enabling a VCTM to be directly docked to the system. Specimens introduced via a VCTM could be inserted directly into the APT analysis chamber via a "piggyback" puck, maintaining the specimen under vacuum and at constant cryogenic temperatures. The sample was analyzed using laser pulsing analysis (35–45 pJ, 80–240 kHz, 1 ion per 100 pulses on average, and 25k base temperature). 3D reconstructions and atom probe data analysis were completed using AP Suite 6.3, a commercially available software from CAMECA Instruments Inc. (Madison, WI, USA).

III. RESULTS AND DISCUSSION

A. *in-situ* synchrotron X-ray analysis of alloying and interphase evolution

1. Baseline characterization of the liquid-cell system

For each experiment, a large-area, low-resolution XRF scan (0.1 s exposure time, 1250 nm step size, 52×155 point scan area) was performed across the entire electrode area, with a representative example shown in Fig. 3(a)(i). The region exhibiting the highest Pt-Lα signal across the electrodes corresponds to the area where the top and bottom SiN_x windows on both chips overlap. For each experiment, this area was chosen for analysis to maximize signal intensity. Figure 3(a)(ii–iii) presents a representative XRF scan (0.1 s exposure time, 50 nm step size, 89×154 point scan area) of this overlapping region before and after electrolyte addition. A clear reduction in XRF signal intensity can be noted, highlighting the challenge of maintaining a sufficient X-ray signal for tracking any changes during subsequent *in-situ* liquid experiments.

XRD patterns (0.1 s exposure time, 50 nm step size, 89×154 point scan area) were acquired from the same region for both the dry and wet electrode and are shown in Fig. 3(b). Multiple Pt reflections were observed, including Pt (111), Pt (200), and Pt (220), confirming the face-centered cubic (fcc) polycrystalline structure of the electrode. The positions of these reflections remained unchanged following electrolyte addition, indicating structural stability of the Pt electrode. However, the overall diffraction intensity dropped, likely due to increased X-ray absorption and scattering by the electrolyte. Despite this drop in intensity, there is still a clear measurable diffraction signal. Additionally, in the regions around $Q = 1.0–1.5$ $Å^{-1}$ and $Q = 3.75–4$ $Å^{-1}$, the wet electrode showed a slight increase in background, which can be attributed to diffuse scattering from the amorphous electrolyte [39]. For each XRD scan, a diffraction pattern was collected at each scan point, and the generated spectrum is the sum of these collective patterns. Representative diffraction patterns from individual scan positions are provided in Supplemental Fig. S1 [35]. Collectively, these findings confirm that the underlying crystallographic structure of the Pt electrode remains unchanged following electrolyte addition.

A representative CV curve for the first lithiation-delithiation cycle, acquired under a voltage range of 2–3 V vs Pt at a scan rate of 0.01 $V s^{-1}$, is shown in Fig. 3(c). The overall shape of the curve indicates that lithiation and delithiation are largely reversible under these biasing conditions. Previous work by Kim *et al*. [40] has shown that lithiation of Pt proceeds via a direct phase transformation to Li_2Pt, followed by a three-step delithiation process involving solid-solution behavior. Consistent with these reports, two anodic features (labeled 1 and 2 in Fig. 3(c)) are observed, corresponding to the reported stepwise phase transformation of Li_2Pt to LiPt. Upon continued delithiation, the system transitions through a solid-solution regime with continuously varying Li content, prior to the formation of $LiPt_2$ and eventual recovery of the parent Pt phase. The presence of these characteristic electrochemical features confirms that the Pt electrode can be effectively biased to monitor phase transitions using this setup. Variations in biasing conditions required to optimize X-ray signal intensity will be discussed in later sections.

Together, the XRF and XRD results for both dry and wet electrodes, along with the first-cycle CV curve, provide essential baselines for interpreting the data presented in subsequent sections. As discussed, the addition of electrolyte to the system reduces both XRF and XRD signal

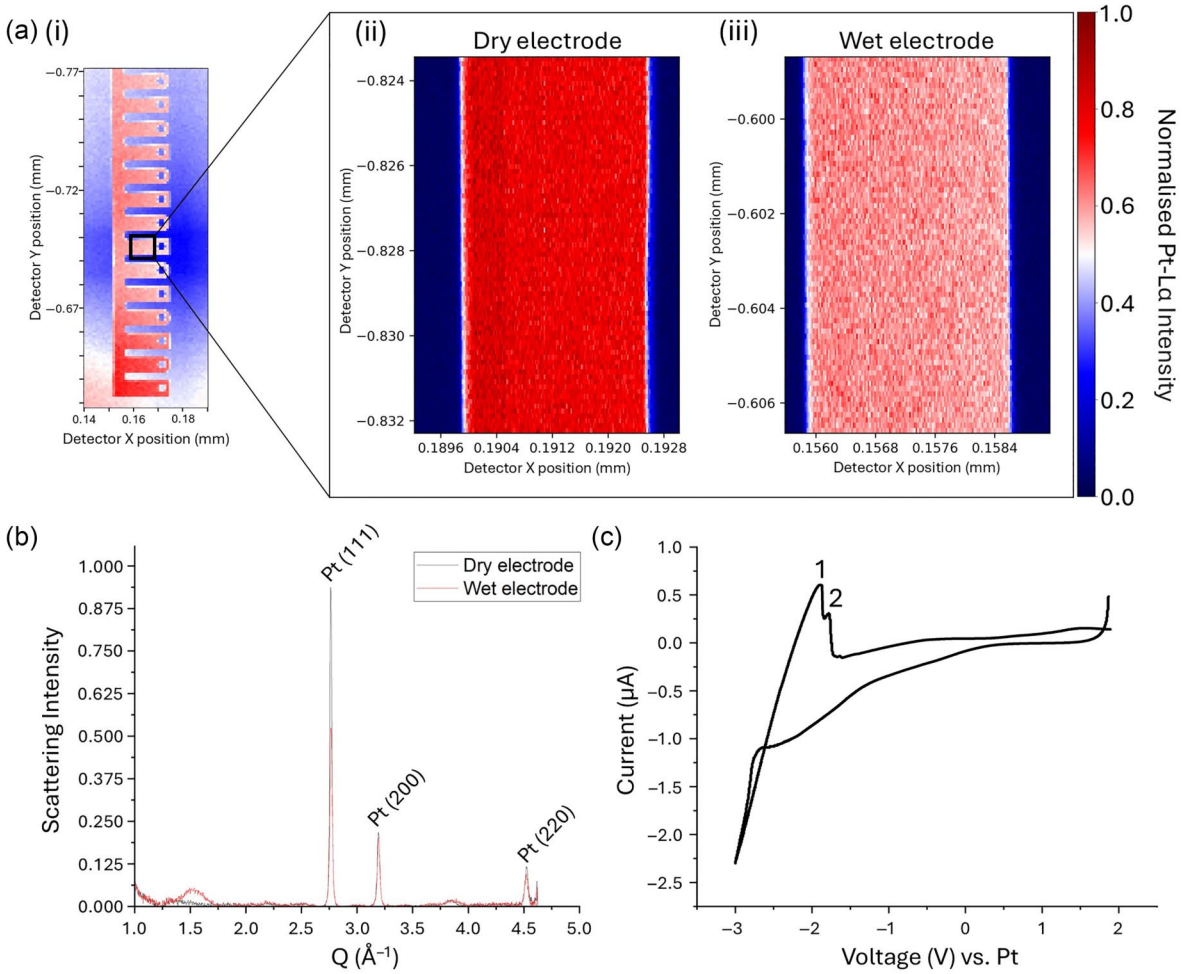

FIG. 3. (a) Representative XRF maps (Pt-Lα) of the electrode region showing: (i) the entire electrode area, with the region of maximum Pt-Lα signal indicated by the black square, (ii) the highlighted region dry and (iii) the highlighted region with electrolyte. (b) Corresponding XRD patterns collected from the same region before and after electrolyte addition, with Pt (111), (200), and (220) reflections labeled. (c) Representative CV for the first lithiation-delithiation cycle of the electrode, biased between 2 and −3 V at a scan rate of 0.01 V/s. Two peaks are labeled 1 and 2, representing the characteristic stepwise phase transformation during early cycling.

intensity, highlighting the general challenge of maintaining sufficient signal under *in-situ* conditions. A complementary comparison in Supplemental Fig. S2 [35] using a similar nanocell setup within a TEM further illustrates characterization challenges in liquid environments. In Fig. S2 (a), a STEM image of a dry electrode is shown, where the polycrystalline grain structure of the system can be clearly imaged. In Fig. S2 (b), the corresponding diffraction pattern for this electrode exhibits distinct rings, confirming the polycrystalline structure. Following the addition of electrolyte, as in Fig. S2 (c), the image resolution decreases significantly, with individual grains no longer easily visible. Further, the diffraction pattern for the wet sample in Fig. S2 (d) shows no clear features, emphasizing the challenges of achieving high-resolution structural characterization in liquid environments using electron microscopy techniques and highlighting the role of X-ray methods.

As a further cautionary note, Supplemental Fig. S3 [35] shows a sample likely contaminated during cell assembly or exposed to air during transport to the beamline. Sharp peaks between Q = 3.25–4 $Å^{-1}$ are evident, indicative of unintended crystalline or semi-crystalline phase formation. These peaks shifted upon biasing, emphasizing the critical importance of clean, airtight sample preparation to prevent artifacts in subsequent XRD and XRF measurements.

2. Lithiation: Formation of alloys and SEI initiation

Figure 4(a) shows *in-situ* XRD datasets (0.1 s exposure time, 50 nm step size, 24 × 54 point scan area) of the Pt anode following lithiation over two separate cycles. A table showing matched species with a tolerance of ±0.015 $Å^{-1}$ for reflections labeled 1–9 is provided in Supplemental Table T1 [35]. The system was biased

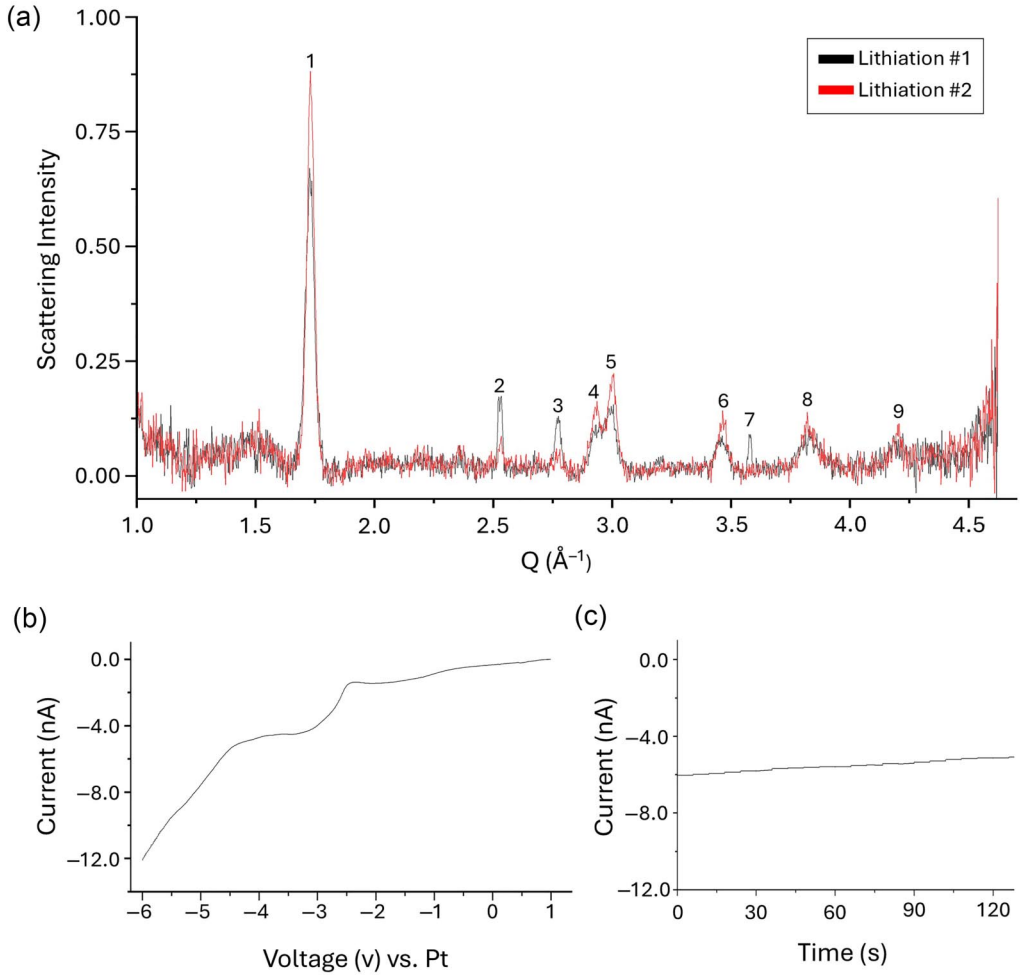

FIG. 4. (a) *in-situ* XRD patterns of the Pt anode following lithiation over two cycles, with the first lithiation shown in black and the second lithiation in red. Notable reflections are labeled 1–9. (b) Electrochemical biasing conditions used during XRD acquisition: (i) voltage sweep from 1 to −6 V at 0.01 V s^{-1} and (ii) corresponding current response vs time during the 130 s hold at −6 V.

from 1 to −6 V at a scan rate of 0.01 V s^{-1}, as shown in Fig. 4(b). For the XRD scan, the potential was held at −6 V for 130 s to ensure the electrode remained in a fully lithiated state throughout the raster acquisition, such that the diffraction patterns acquired at each position correspond to a consistent alloyed phase. The current remained stable throughout this hold, as shown in Fig. 4(c). The potential implications of these aggressive cycling conditions are discussed in A5.

In both cases, the formation of a Pt-Li alloy, Li_2Pt, was observed, corresponding to peaks 1, 4, 5, 6, 8, and 9 in Fig. 4(a). During lithiation, the fcc Pt structure transformed into a hexagonal Li_2Pt-type structure, consistent with previous reports [40]. Multiple reflections are detected, including Li_2Pt $(10\bar{1}0)$, Li_2Pt $(10\bar{1}1)$, Li_2Pt $(11\bar{2}0)$, Li_2Pt $(20\bar{2}0)$, Li_2Pt $(11\bar{2}1)$, and Li_2Pt $(20\bar{2}1)$, consistent with the polycrystalline nature of the electrode.

During the initial lithiation cycle, in addition to the Li_2Pt alloying peaks, several additional reflections were detected, each with potential overlapping assignments. Peak 3 corresponded to the Pt (111) reflection. The persistence of this reflection during the first cycle suggests that the lithiation capacity was insufficient to fully alloy the Pt anode at this stage. In contrast, during the second lithiation cycle, the Pt (111) reflection disappeared, while the Li_2Pt alloying peaks (1, 4, 5, 6, 8, and 9) exhibited increased scattering intensities, indicating a more complete alloying process. Peaks 2 and 7 were consistent with the bcc Li (110) and Li (200) reflections, respectively. The presence of metallic Li likely indicates Li plating on the anode surface during early lithiation. This behavior is particularly common under aggressive intermediate overpotentials or when the SEI is incomplete or unstable. The formation of Li cauliflower deposits under these conditions, consistent with uneven Li nucleation and incomplete SEI formation, has been reported previously using LCTEM [9,13]. However, determining the exact origin of the Li signal is challenging based on XRD alone, highlighting the complementary role of operando LCTEM imaging.

During the second lithiation cycle, the Li (200) reflection was no longer resolved. The remaining Li (110) reflection exhibited significant overlap with a nearby Li_2CO_3 (020) reflection, and Li_2CO_3 also presented potential overlaps with peaks 3, 6, and 9. Li_2CO_3 has been reported as a major component of the inner SEI layer of Pt alloying anodes during early cycling, supported by correlative nanoscale compositional analysis in previous studies [9,40]. The catalytic properties of metals like Pt are known to accelerate the decomposition of electrolyte solvents such as EC, particularly in the presence of trace water or HF, leading to enhanced formation of Li_2CO_3 and LEDC as initial SEI components [41,42]. Li_2CO_3 has limited stability within the SEI, and previous work has shown that Li_2CO_3 can be reduced to Li_2O and gaseous species such as CO or CO_2 under aggressive electrochemical conditions [43,44]. SEI cracking and mechanical instability during early cycles are also commonly observed in high-capacity alloying anodes such as Si, where large volume changes induce fracture and reformation of the SEI layer, particularly when the electrode is not fully passivated during early cycling [9,45].

While definitive assignment of Li_2CO_3 based solely on XRD should be interpreted with caution, the disappearance of the Li (200) reflection, the emergence of overlapping reflections in subsequent cycles, and complementary nanoscale compositional evidence collectively support the presence of carbonate-derived SEI components during early lithiation [9]. In this context, this work provides one of the first nanoscale spatially resolved hard X-ray XRD studies capturing Li metal, alloying peaks and SEI-related reflections under liquid cell conditions at an anode-electrolyte interface.

3. Delithiation: Reversible dealloying and solid-solution reaction

Following lithiation and the formation of Li_2Pt alloying reflections, the system was returned to 0 V. A subsequent XRD dataset (0.1 s exposure time, 50 nm step size, 24×54 point scan area) was acquired, as shown in Fig. 5(a) and compared with the second lithiation dataset. Supplemental Table T2 [35] provides matched species with a tolerance of ± 0.015 $Å^{-1}$ for reflections labeled A and B. Notably, the multiple Li_2Pt reflections were replaced by a single broad LiPt (0001) reflection, labeled A in Fig. 5 (a). The persistence of a Li-Pt alloying phase following delithiation is consistent with incomplete Li extraction.

Significant peak broadening was observed, indicative of increased lattice strain and reduced crystallite domain size during delithiation. This broadening may also reflect mechanical stresses and microstructural changes arising from repeated alloying and dealloying cycles. Previous studies report that residual Li can become trapped within the Pt lattice [9,40], hindering a full return to the original Pt structure. Incomplete delithiation is consistent with kinetic barriers associated with lattice strain and Li diffusion limitations, as evidenced by the persistence of LiPt reflections after cycling.

The broadening and persistence of LiPt peaks also indicate a transition in the dealloying mechanism. This behavior is illustrated in Fig. 5(b), which compares baseline electrochemical data from Fig. 1(c) with data obtained after more than 20 cycles. The merging of anodic peaks signifies a shift from discrete phase transformations to a more solid-solution-like reaction mechanism [40]. These structural evolutions influence Li diffusion kinetics and have important consequences for the mechanical stability and electrochemical performance of Pt-based alloy electrodes during cycling.

In addition to the LiPt (0001) reflection, the Li_2CO_3 (020) reflection persists (labeled B in Fig. 5(a)) and exhibits increased intensity relative to the lithiated state. This increase may arise from repeated alloying-induced volume changes and associated lattice strain, which can change grain orientation and bring additional crystallites into Bragg condition, increasing the measured XRD intensity without necessarily altering the actual thickness or composition of the SEI. Structural rearrangements within the anode during delithiation may also expose fresh surfaces to the electrolyte, promoting further electrolyte decomposition and thereby increasing the observed Li_2CO_3 signal. Together, these observations indicate a dynamic and evolving interphase that responds to electrochemical cycling.

Simultaneous XRF measurements (0.1 s exposure time, 50 nm step size, 77×178 point scan area) of both the lithiated and delithiated states further highlight the ongoing microstructural evolution in terms of elemental density. While the spatial distribution of the Pt-Lα signal showed no obvious change during early cycling (Supplemental Fig. S4 [35]), a clear difference in intensity was observed. As shown in Fig. 5(c), the delithiated state produced a higher XRF signal than the lithiated state. At the incident energy used in this study, the attenuation length of Pt Lα fluorescence ($\sim$9.44 keV) in Pt is on the order of several micrometres [46], substantially larger than the $\sim$50–150 nm thickness of the patterned Pt electrode. The detected fluorescence signal therefore integrates over the full electrode thickness, and the observed variation in intensity cannot be attributed to changes in the total Pt content. Instead, the variation is consistent with lithiation-induced lattice expansion and delithiation-induced contraction of the Pt-Li alloy, together with associated microstructural changes that modify the spatial distribution of Pt within the probed volume. Such lattice expansion during lithiation has been directly visualized in real time in previous studies [9,13], lending further support to the structural interpretation presented here.

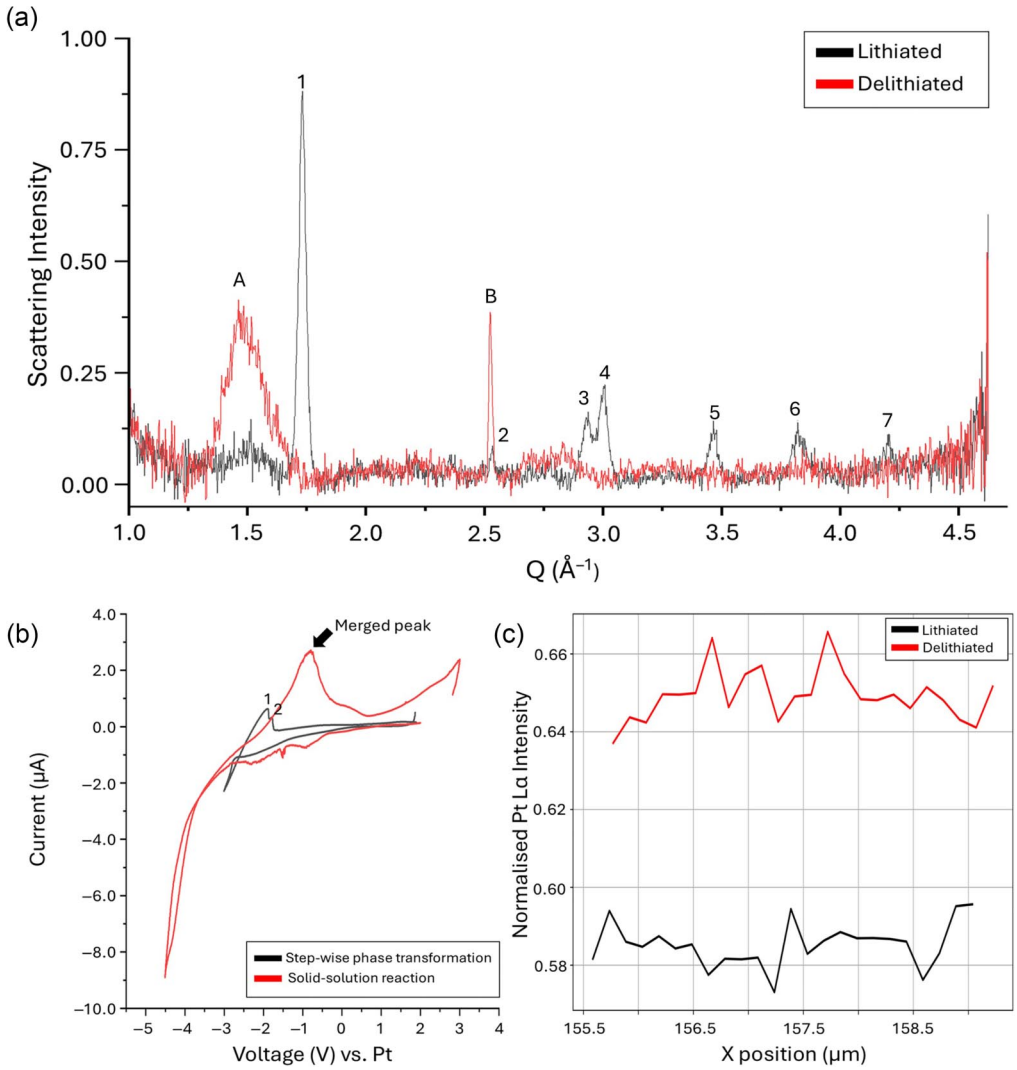

FIG. 5. (a) *in-situ* XRD patterns of the electrode in the lithiated (black) and delithiated (red) states. Notable delithiation-related reflections are labeled A and B, while lithiation-related reflections are labeled 1–7. (b) Comparison of electrochemical profiles from the initial baseline and after more than 20 cycles, showing the progressive merging of anodic peaks 1 and 2 into a single feature. (c) Normalized Pt-Lα intensity as a function of x-position for the lithiated (black) and delithiated (red) states.

4. Long-term cycling: SEI evolution and electrode redistribution

To evaluate the evolution of interfacial components and electrochemical behavior under extended cycling, the same electrode was subjected to a total of 50 charge-discharge cycles (0.2 V s^{-1}, 3 V to −4.0/4.5 V), with intermittent simultaneous XRF and XRD scans (0.1 s exposure time, 200 nm step size, 37 × 194 point scan area) performed after selected cycles. Figure 6(a) presents the combined XRD datasets following a number of these cycles. Supplementary Table T3 [35] provides matched species with a tolerance of ±0.015Å^{-1} for reflections labeled C and D. Within the datasets, a reflection consistent with Li_2CO_3 (020) (labeled B) persists, albeit diminishing with increasing cycles. Additionally, an emerging SEI reflection consistent with LiF (200) (labeled D) is observed. LiF is widely recognized as a key stabilizing component of the inner layer of the SEI in many LIB studies [2,47,48] and has also been reported as part of the SEI on Pt-based alloy anodes [40].

Figure 6(a) shows the continued persistence of the LiPt (0001) reflection (labeled A) even following extended cycling. Notably, the scattering intensity of this peak gradually increases before stabilizing. This increase in intensity likely reflects structural changes within the electrode, such as increased crystallinity or improved phase homogeneity, factors known to enhance the diffraction signal, as observed in other *in-situ* X-ray studies of alloy anodes [49–51]. Concurrently, the LiPt (0001) peak shifts from approximately 1.490 to 1.510 Å^{-1} in Q-space, denoting lattice contraction, pointing towards subtle changes in the lattice parameters, which can be attributed

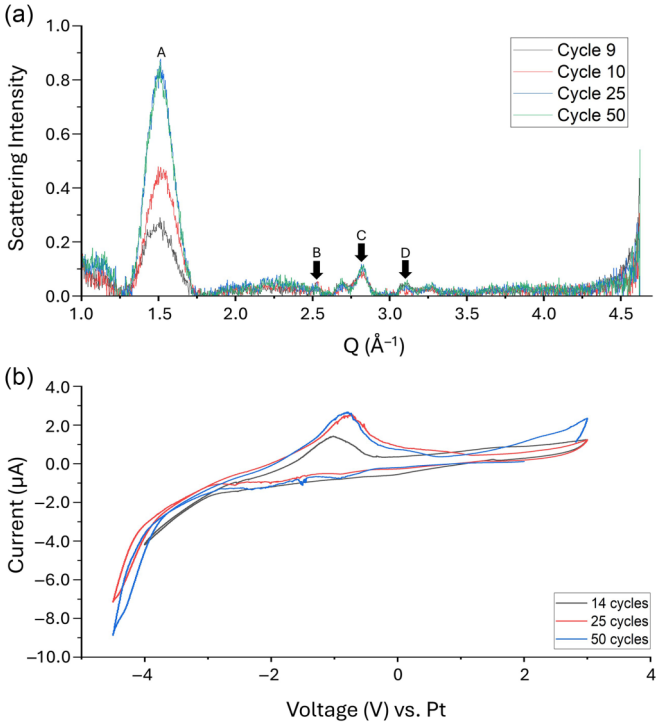

FIG. 6. (a) *in-situ* XRD patterns collected after selected cycles during 50 charge-discharge cycles, with notable reflections labeled A–D. (b) CV curves recorded at selected cycle numbers during extended cycling.

to strain relaxation, phase reordering, or gradual changes in Li content within the alloy, consistent with prior reports on phase evolution in alloy electrodes during Li insertion [52,53]. Additionally, the emergence of a reflection consistent with $LiPt_7$ (222) (labeled C) is observed with cycling, suggesting further phase evolution and increasing complexity in the alloying mechanism. Following this period, the system reaches a steady state, where both the Q-value and peak intensity of the LiPt (0001) reflection remain consistent, signifying stabilization of the electrode structure and Li distribution. These observations highlight an initially dynamic cycling evolution, followed by sustained structural stability, which is critical for the long-term performance of the Pt-based anode.

Figure 6(b) shows the electrochemical biasing curves acquired over multiple cycles. A single peak in the anodic part of the cycle persists throughout, consistent with a solid-solution-type reaction mechanism. With continued cycling, this peak gradually shifts toward lower voltages, reflecting increasing polarization and overpotential. Despite this shift, characteristic lithiation and delithiation features remain consistent after extended cycling, indicating that electrochemical activity is maintained, albeit with evolving kinetics. Additionally, the anodic peak intensity increases over time, which may reflect improved utilization of the electrode material or progressive changes in reaction pathways [54].

To further substantiate the transition toward a solid-solution-like reaction mechanism, the evolution of the LiPt (0001) reflection was quantified as a function of cycle number (Supplemental Fig. S5 [35] and Supplemental Table T4 [35]). The peak position shifts from $Q \approx 1.49$ Å^{-1} at early cycles (e.g., cycle 8) to a constant value of $Q \approx 1.51$ Å^{-1} after ~14 cycles, consistent with progressive lattice relaxation and subsequent stabilization of a single LiPt phase. Over the same range, the LiPt (0001) FWHM is largest in the early cycles and converges to ≈0.28–0.29 Å^{-1} beyond ~14 cycles, indicating reduced lattice strain and an increasingly homogeneous alloyed microstructure. These structural trends correlate with the electrochemical response, where the two distinct anodic peaks observed in the initial cycles merge into a single broader peak after extended cycling [Fig. 6(b)], indicative of a solid-solution-type process rather than discrete phase transformations [40]. Taken together, the systematic evolution and subsequent stabilization of the LiPt (0001) peak position and FWHM, combined with the merged anodic feature in the CV profiles, provide quantitative evidence for a gradual transition from discrete phase transformations to a solid-solution-like reaction mechanism in the Li-Pt alloy anode during prolonged cycling.

Figure 7 presents the corresponding XRF datasets of the Pt electrode over extended cycling, acquired simultaneously with the XRD in Fig. 6 at the end of each cycle following delithiation. Over time, pronounced changes are observed in both the distribution and intensity of the Pt-Lα signal. After 10 cycles, there is a notable decrease in Pt-Lα intensity across the electrode, consistent with continued alloying and associated changes in local elemental density. By 15 cycles, significant redistribution of the Pt signal occurs, with distinct voids appearing within the electrode structure and Pt migrating towards the edges and corners. The redistribution of the Pt and the formation of these voids intensify with further cycling, indicating progressive microstructural reorganization of the electrode during prolonged alloying-dealloying [9].

Further to this, it has been shown that Pt may migrate as a result of stress-driven diffusion or electrochemical dissolution and re-deposition processes, consistent with the redistribution observed here [55,56]. The redistribution of Pt towards edges and corners of the electrode, as in the red areas in Fig. 7 (cycles 16–50), may be influenced by intensified local electric fields at these geometrical features [13]. Such enhanced fields can accelerate Pt dissolution and promote its migration and redeposition preferentially at edges and corners. Combined with mechanical stresses from repeated cycling, this contributes to the evolving electrode morphology and highlights the challenges in preserving electrode stability over long-term operation.

Importantly, despite these morphological changes and the observed redistribution of Pt, electrochemical

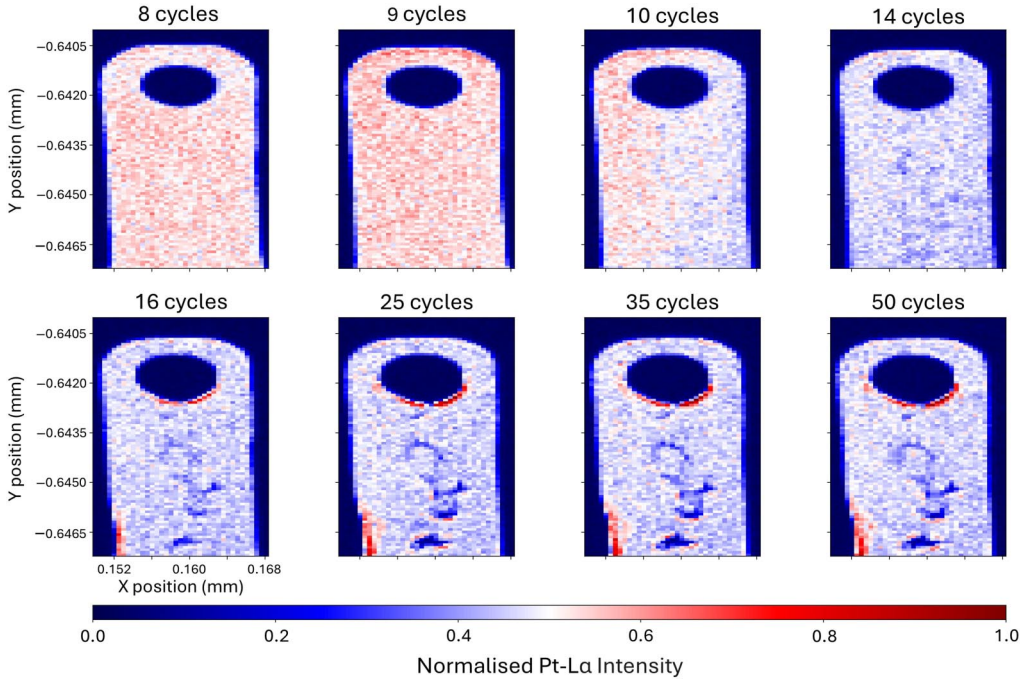

FIG. 7. Normalized Pt-Lα XRF intensity maps after selected cycles following delithiation, showing changes in Pt distribution and intensity across the electrode during extended cycling.

activity remains sustained, with characteristic lithiation-delithiation features preserved [Fig. 6 (b)]. This sustained electrochemical activity is consistent with the persistence of the active LiPt (0001) reflection [labeled A in Fig. 6 (a)] throughout cycling and the concurrent emergence of stabilizing SEI components such as LiF. While this redistribution and the mechanical stresses associated with repeated volume expansion would be expected to compromise the integrity of the fragile SEI layer, it appears to remain effective due to its dynamic nature, continuously breaking down and reforming to preserve electrode passivation.

The SEI evolution observed in this study involving early-cycle Li_2CO_3 formation followed by LiF is consistent with a dynamic, self-renewing interphase. As mentioned, Li_2CO_3 has been shown to be unstable under repeated cycling, while LiF accumulation is frequently reported as a stabilizing component that lowers interfacial impedance and enhances passivation [47,48,57]. Similarly, the transition from a stepwise alloying-dealloying pathway to a solid-solution type reaction mechanism centered on LiPt likely reflects a mechanistic shift toward phase regimes that better accommodate strain and support reversibility [19,40]. Together, these trends suggest that sustained electrochemical performance in this system is enabled by the continuous renewal of the interphase in conjunction with a solid-solution alloying mechanism. While demonstrated here for a Pt-based alloy anode, such behavior is likely relevant to other alloy and conversion anodes that undergo large volume changes and rely on dynamic interphase formation for stability.

5. Influence of confined electrochemical conditions on alloying and SEI evolution

The relatively large overpotentials applied during *in-situ* measurements and their potential influence on the observed phenomena warrant consideration. In contrast to the baseline electrochemical curve shown in Fig. 3(c), the system was driven from −3 to −6 V to generate a sufficient alloying signal for XRD detection. This shift can be attributed to several factors, most notably due to the confined electrolyte volume within the nanocell.

First, concentration polarization arises because the confined electrolyte volume promotes rapid local depletion of Li^+ ions and alters the local cosolvent ratio near the Pt working electrode, even at moderate current densities [58]. To sustain lithiation under these conditions, larger overpotentials are required. Second, slow replenishment of Li^+ ions from the bulk electrolyte exacerbates this effect, as diffusion pathways are constrained within the nanocell geometry, reducing the ability of the bulk to supply ions to the electrode surface [59,60]. Finally, electrolyte resistance also plays a role. Despite reasonable ionic conductivity, the small electrolyte volume can exhibit increased effective ohmic resistance, particularly when ionic path lengths are extended or cross-sectional areas are restricted, leading to increased voltage losses during cycling [61].

During the lithiation sweep, the geometric current density is estimated to be ≈ 0.33 mA cm^{-2} (Fig. 4(b)), decreasing to ≈ 0.16 mA cm^{-2} during the subsequent voltage hold (Fig. 4 (c)). These values are comparable to low-rate cycling in practical batteries. However, in the strongly

confined liquid cell geometry used here, they act on an extremely small electrolyte volume. As a result, even modest geometric current densities can generate significant concentration polarization and local Li^+ depletion, promoting electrolyte decomposition, SEI growth, and Li plating at the Pt surface. The high apparent overpotentials (down to −6 V vs Pt) should therefore be viewed as a consequence of geometry-induced transport limitations, while the underlying alloying pathway and SEI evolution are consistent with mechanisms expected under more conventional low-rate cycling conditions.

In addition to these volume-related effects, gas evolution during cycling may generate bubbles within the confined electrolyte, partially blocking electrode surfaces and further restricting mass transport [62,63]. This effect is particularly detrimental in nanocell volumes where the effective transport cross section is already limited. Solvent evaporation arising from imperfect sealing of the electrochemical cell may also contribute to reducing electrolyte availability and contribute to sluggish ion transport [64,65]. As Pt-based alloying phenomena are capacity-dependent [40], reaching the critical capacity for alloying necessitates increasing the applied potential to compensate for these limitations. Despite applying −6 V in the first lithiation cycle, Pt reflections persist, highlighting challenges associated with achieving complete alloying under confined conditions.

The effect of holding the voltage at −6 V for 130 s warrants careful consideration. The relatively stable current during this hold suggests that a quasisteady-state lithiation process was established. This suggests that Li^+ ion transport was sufficient to sustain continued alloy formation under these conditions. While parasitic side reactions and Li plating occurring in parallel cannot be fully excluded, the absence of strong current fluctuations suggests that abrupt or unstable processes were not dominant. Furthermore, the relatively short hold time should minimize the extent of any competing steady-state side reactions. Together, these observations indicate that the system remained sufficiently stable to support controlled alloying under these conditions.

Although the applied potentials exceed those typically used in conventional battery testing, they were required to overcome the intrinsic mass-transport and resistance limitations of the confined electrolyte environment. The combination of a controlled −6 V hold and stable lithiation current enabled the formation and detection of Pt-Li alloy phases with sufficient signal while avoiding catastrophic electrode degradation. This balance allowed clear observation of the alloying mechanisms while preserving the overall structural and electrochemical integrity of the MEMS cell.

Notably, the long-term cycling shown in Fig. 6(b) was conducted within a more moderate potential window (−4 to −4.5 V vs Pt), with −6 V only applied during short holds for XRD/XRF measurements. For the long-term cycling case, the geometric current density is estimated to be ≈0.19–0.24 A cm^{-2}, corresponding to absolute currents of only ∼7–9 μA. Such current densities are higher than those typically employed in commercial cells, placing the nanocell in a strongly driven, transport-limited regime. Under these conditions, electrolyte decomposition, SEI thickening and Pt redistribution are expected to proceed more rapidly than under practical operating conditions. Therefore, the observed morphological changes and SEI growth should be interpreted as an accelerated, upper-bound scenario. Nevertheless, the persistence of a LiPt-dominated alloy phase and the gradual transition from a carbonate-rich to LiF-rich SEI during this high-rate cycling suggest that the fundamental alloying and interphase-evolution mechanisms remain consistent.

B. Correlative cryogenic microscopy

1. Cryogenic FIB/SEM imaging and cryogenic sample preparation of cycled electrodes

Following the *in-situ* liquid cell synchrotron XRD and XRF experiments, the MEMS nanochips were frozen and transferred to the cryo stage of a PFIB/SEM for further analysis [26]. Figure 8(a) shows an SEM image of a preserved section of the frozen liquid-solid interface between the electrode and the electrolyte. A relatively thick electrolyte layer covers several electrodes, highlighted by white arrows. The thickness of the frozen electrolyte layer limited detailed structural analysis of the underlying electrode. However, this image confirms that the liquid-solid interface was successfully preserved throughout disassembly, transfer and freezing from the synchrotron to the cryogenic PFIB/SEM.

Supplemental Figure S6 [35] shows attempts made to create a lift-out from this electrolyte-covered region. Milling through the SiN_x window revealed a thick layer of electrolyte covering the ROI, which complicated reliable identification of the underlying electrode. Evidence of membrane window bulging and partial delamination was also observed, likely arising from mechanical stresses induced by repeated volume changes of the Pt electrode during aggressive lithiation-delithiation cycling. While these effects indicate mechanical degradation of the MEMS cell, their precise impact on interfacial integrity could not be resolved from SEM imaging alone. Consequently, these regions were not selected for site-specific specimen preparation.

Instead, a region where the electrode was partially exposed was used for further analysis, allowing direct observation of the structural consequences of long-term cycling, as shown in Fig. 8(b). Multiple voids were evident across each of the electrodes, as well as accumulation of material along the edges, most likely Pt, as highlighted in the XRF data shown in Fig. 7. While the electrochemical

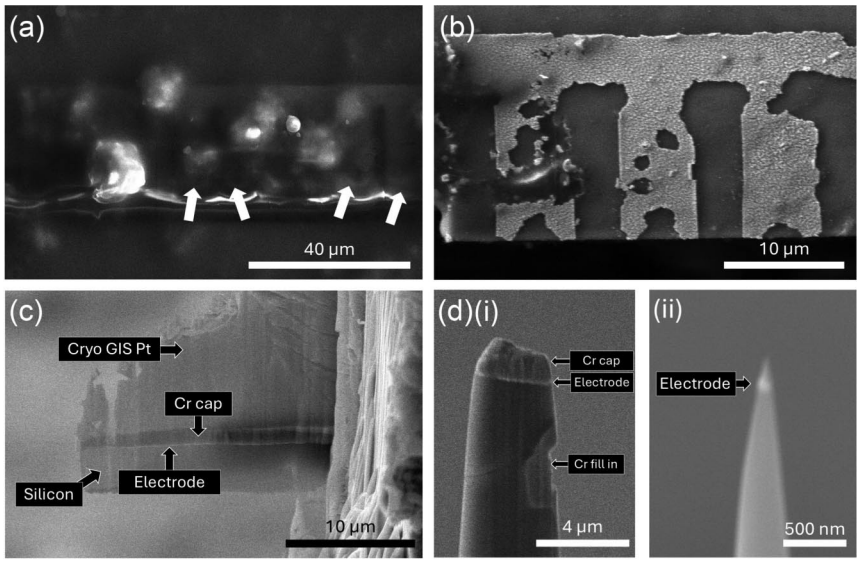

FIG. 8. (a) SEM image (30 kV, 1.6 nA) of electrodes, highlighted by the white arrows, buried beneath the electrolyte layer. (b) SEM image (10 kV, 0.4 nA) of a partially uncovered electrode after long-term cycling. (c) SEM image (20 kV, 1.6 nA) of a TEM lamella with visible Cr protection cap, cryogenic GIS Pt cap and electrode prepared using Ar plasma. (d) SEM images (10 kV, 0.4 nA) of the cryo-APT sample preparation: (i) a lifted-out electrode on a post with a visible Cr protection cap and Cr fill in and (ii) a final thinned needle specimen containing the electrode.

performance of the electrodes remains largely stable over cycling (Fig. 6(b)), the extent of structural damage observed here highlights challenges associated with maintaining electrode integrity under prolonged cycling conditions, which are particularly detrimental for industrial-relevant applications where electrode stability is key.

To further investigate the effects of long-term cycling on the structure of the electrode and SEI composition at higher spatial resolution, a portion of the exposed electrode was coated with Cr, lifted out and prepared into both a cryo-TEM lamella and a cryo-APT specimen for analysis, as shown in Figs. 8(c) and 8(d). For cryo-STEM preparation, the Cr-coated area was further capped with nonsite-selective GIS Pt, lifted out using redeposition welding and attached to a Mo lift-out grid. Initial thinning was performed using Xe plasma milling, followed by final thinning with Ar plasma. The completed lamella is shown in Fig. 8(c) where the protective layers and the electrode interface are clearly visible. The TEM lamella was transferred back into the inert glovebox using a VCTM and mounted into a Melbuild vacuum-transfer TEM holder. The holder tip was retracted prior to removal from the glovebox to prevent exposure to the ambient atmosphere. The holder was then inserted into the TEM, and the sample tip was only extended once the rod was inside the TEM column and under a vacuum better than 10^{-8} mbar. Cryo-APT specimen preparation largely followed the methodology outlined by Mulcahy *et al.* [26]. Figure 8(d) (i) shows a mounted sample on a Si microarray post, while Fig. 8 (ii) shows the final Xe plasma-thinned needle-shaped specimen, with the electrode clearly captured within the tip. Detailed preparation parameters for cryo-APT are provided in Supplemental Fig. S7 [35].

2. Cryo-STEM EDX and EELS mapping of solid-electrolyte interphase

Figure 9(a) presents a HAADF-STEM image of the prepared TEM lamella at cryogenic temperatures. Cryo-EDX analysis was conducted on this region with key elements mapped onto the ROI in Fig. 9(b), including F, Si, Pt, and Cr. Elemental maps for additional detected elements including O, C, N, P, and Xe are provided in Supplemental Fig. S8 [35].

From these maps, it is evident that the Pt electrode was successfully captured within the TEM lamella, along with the sputtered Cr protection layer, Si nanochip, and SiN_x window. Notably, a distinct region between the Cr and Pt layers shows a marked absence of these detectable species, which is attributed to the presence of the SEI. This region is spatially heterogeneous and, in some areas, absent, indicating that even after extended cycling, complete and uniform passivation of the Pt electrode surface remained challenging. Furthermore, the electrode exhibits a markedly uneven morphology, with signs of delamination visible in additional cryo-STEM images in Supplemental Fig. S9 [35], underscoring the effects of prolonged cycling on surface integrity and morphology. The electrode is clearly polycrystalline, as evidenced by the Fourier transform shown in Fig. 9(c). Additional 4D-STEM data were acquired to further confirm the polycrystalline nature of the electrode, as shown in Fig. 9(d).

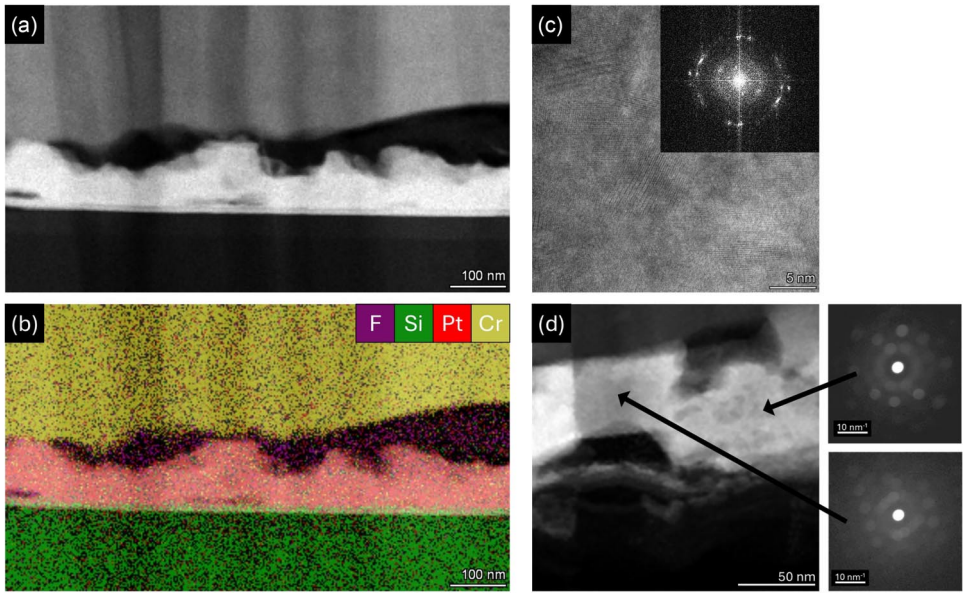

FIG. 9. (a) HAADF STEM image of the prepared TEM lamella. (b) EDX map of the same region showing signals corresponding to F (pink), Si (green), Cr (yellow), and Pt (red). (c) Lattice resolution STEM with Fourier transform insert of image and (d) STEM image from 4D-STEM data set with diffraction patterns shown from different regions of the area imaged.

To further probe the composition of the identified SEI layer, cryo-EDX maps of typical SEI components, including F in Fig. 9(b) and P, C, and O in Supplemental Fig. S8 [35] were examined. These maps reveal that the SEI region is enriched in F-containing species, with a near-absence of C and a reduced O signal. While EDX alone cannot uniquely determine the chemical form of fluorinated species and minor contributions from F-containing polymers cannot be fully excluded, this distribution is consistent with a LiF-rich interphase and a substantial reduction of carbonate-derived species.

To corroborate this observation, cryo-STEM-EELS analysis was conducted on the SEI region and is presented in Fig. 10. The cryo-EELS spectrum in Fig. 10(a) exhibits a deviation from the expected Li K-edge at 55 eV, displaying a characteristic double-peak feature between ≈60–75 eV. Comparison with previously reported reference SEI spectra indicates a close correspondence with signatures characteristic of LiF [66–68]. Mapping this signal onto the ROI in Fig. 10(c) demonstrates that the LiF signal is localized exclusively within the region between the Pt and Cr layers. Supplemental Fig. S10 [35] presents a high-loss range showing no detectable O K-edge within the SEI region. This observation indicates a substantial reduction of oxygen-containing species within the interphase. The absence of detectable oxygen also suggests successful transfer from Diamond Light Source to Imperial College London, and from cryogenic FIB/SEM preparation

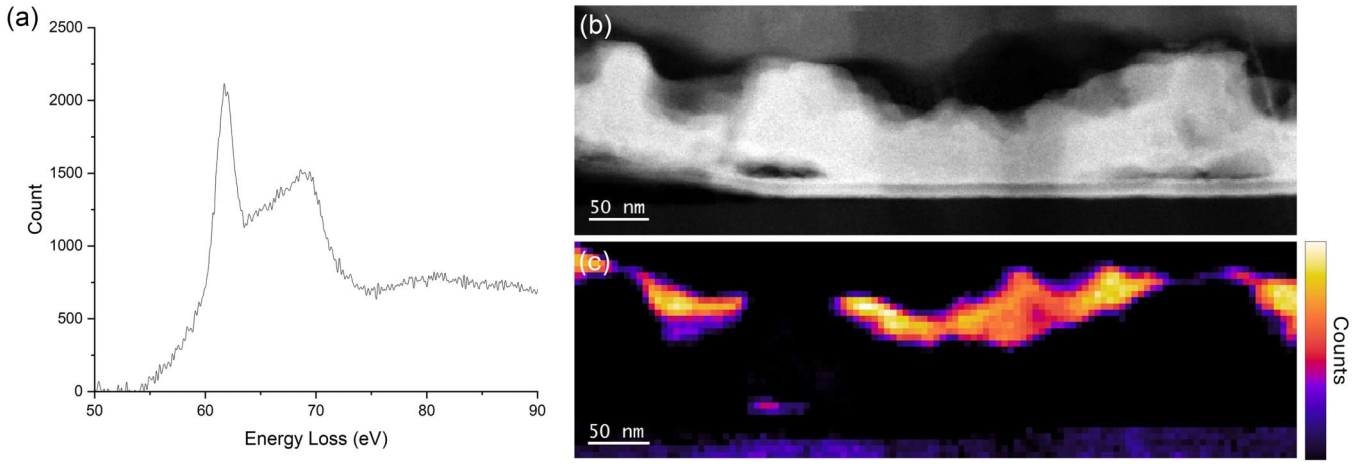

FIG. 10. (a) EELS spectra showing energy loss (eV) vs counts over the 50–90 eV range. (b) HAADF-STEM image of the ROI. (c) Map of the relative EELS signal intensity within the same ROI.

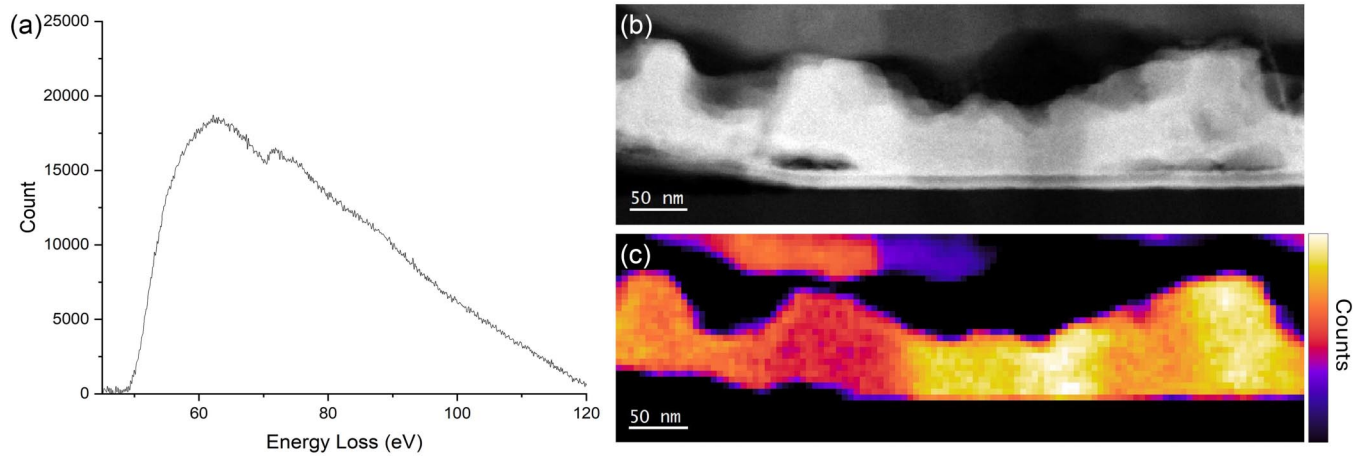

FIG. 11. (a) Cryo-EELS spectrum collected from the electrode region. (b) Cryo-HAADF-STEM image of the ROI, with corresponding EELS signal mapped onto the ROI in (c).

to the TEM, without significant air-induced alteration. Collectively, these findings provide evidence that the SEI evolves from early-stage, unstable carbonate species to a more stable, LiF-dominated interphase, consistent with the enhanced long-term cyclability of the electrode.

To further assess the impact of alloy formation and cycling on the anode structure, cryo-EELS analysis was conducted on a region containing the electrode, as shown in Fig. 11(a). The spectra reveal a pronounced absence of Li-related signals, with the only significant edges corresponding to Pt–O (52 eV) and Pt–N (71 eV). Mapping the EELS signal onto the ROI confirms that the detected signal is confined entirely to the electrode region previously identified by cryo-EDX in Fig. 9. Although *in-situ* XRD measurements (Fig. 6(a)) indicate that the electrode should be composed of a LiPt alloy, capturing Li signals within the electrode proved challenging under these conditions.

Supplemental Figure S11 [35] provides a position-intensity map of the relative inelastic mean-free path across the cryo-HAADF-STEM image in Fig. 10(c). This map reveals significant variations in sample thickness, particularly between the SEI and the electrode. This variation likely arises from differences in milling rates between the beam-sensitive SEI components and the alloying anode during cryogenic sample preparation. These thickness variations complicate the preparation of a uniformly thin lamella, making simultaneous detection of Li in the electrode and reliable characterization of the SEI difficult. To overcome these limitations and more accurately determine compositional variations within the anode, cryo-APT was performed on the electrode.

3. Nanoscale compositional analysis of the electrode via cryo-APT

Figure 12(a) shows the full 3D reconstruction of the cryo-APT specimen prepared in Fig. 8(d). The reconstructed volume can be divided into three distinct regions: a Cr protective coating at the top, a central electrode region containing Pt and Li, and a lower region dominated by Si. Focusing on the electrode, Fig. 12(b) presents 2D contour plots of the relative concentrations of Li- and Pt-containing species in the X-Z orientation. Within the analyzed volume, the detected ion counts of Li (14,412) and Pt (14,984) are low but nearly equal, consistent with the expected stoichiometry of the LiPt phase. Li- and Pt-containing species appear in close proximity but do not strongly overlap spatially, instead forming adjacent regions. Figure 12(c) provides a 1D concentration profile along the Z-axis of the electrode, revealing two compositional regimes.

In Region 1, a clear separation between Pt-rich and Li-rich zones is observed at the interface, indicating significant compositional inhomogeneity and potential nanoscale segregation. This heterogeneity is evident from the steep decline of Pt concentration from nearly 100-at.% to below 20-at.% along the 1D profile, accompanied by a sharp increase in Li concentration. Li concentrations in this region exceed the stoichiometry of equilibrium Li-Pt phases and should therefore be interpreted as transient, nonequilibrium enrichment at the reaction front, rather than as a stable bulk phase. Such compositional gradients at electrochemical reaction fronts are consistent with phenomena reported in alloying anodes where Li diffusivity limitations and mechanical stresses generate dynamic, compositionally diffuse interfaces [69,70]. These local heterogeneities likely emerge from kinetic competition between Li incorporation flux and Pt atom rearrangement near the SEI, facilitating strain accommodation and mitigating volume expansion during lithiation [71,72].

By contrast, in Region 2, located deeper within the electrode, the 3D reconstruction shows a more homogeneous spatial distribution of Pt and Li ions. The compositional maps and profiles indicate reduced nanoscale segregation or clustering, consistent with a relatively

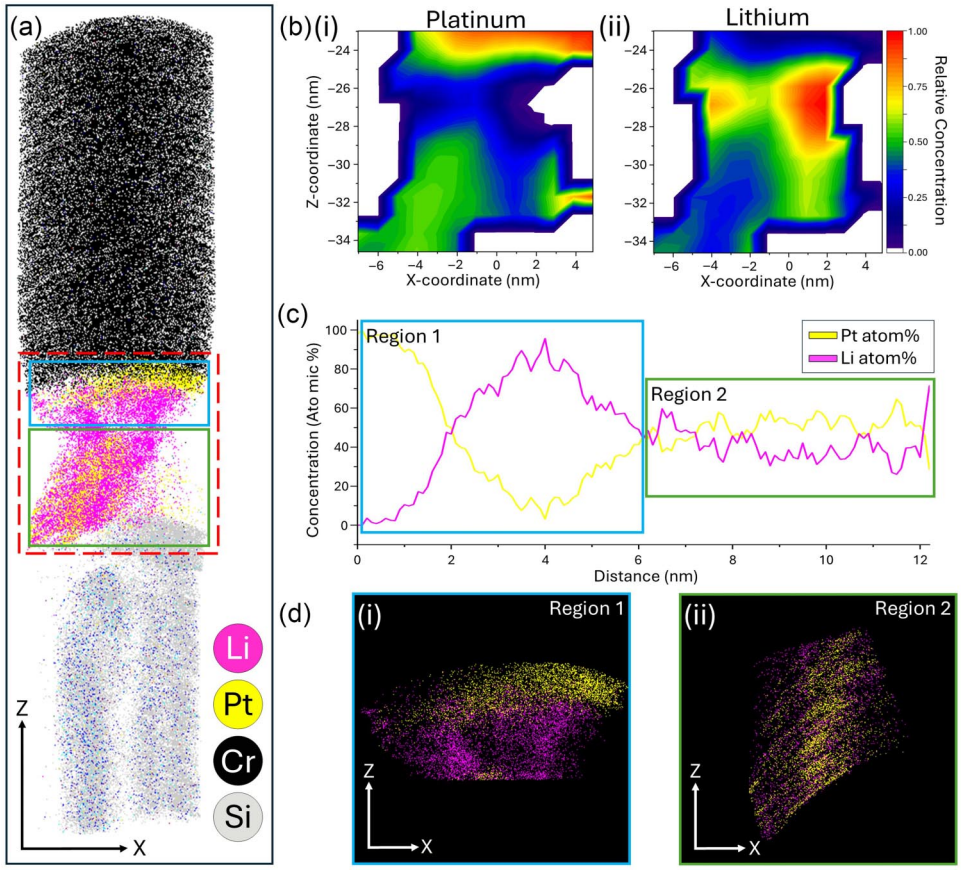

FIG. 12. (a) Full 3D cryo-APT reconstruction, highlighting the Cr protective coating (black), Li (pink), and Pt (yellow) from the Li-Pt electrode and Si (gray). (b) 2D contour plot showing the relative concentration of (i) Li-containing and (ii) Pt-containing species with the red dashed square in (a). (c) 1D concentration profile along the Z-axis of the electrode, showing two compositional regions, highlighted in blue (Region 1) and green (Region 2) in (a). (d) Isolated reconstructions of both regions showing (i) the spatial separation between Pt-rich and Li-rich zones in region 1 and (ii) the more homogeneous Li-Pt distribution deeper within the electrode.

uniform alloying state in this region, with a composition close to 50:50 that corresponds to the LiPt phase identified in the XRD data in Fig. 6(a). Based on the established phase diagram of the Li-Pt system, the stoichiometric LiPt phase is expected to be an ordered intermetallic line compound under equilibrium conditions exhibiting long-range atomic order between Li and Pt ions [73,74]. While difficult to directly resolve atomic ordering with the APT data, the observed compositional uniformity in Region 2 supports the presence of a well-mixed alloy phase without significant nanoscale compositional segregation. The corresponding 3D reconstructions for these two regions are shown in Fig. 12(d).

Compositional gradients of Li and host metal species are a well-established feature of alloying anodes and reflect their intrinsic reaction kinetics [75]. Similar Li-metal gradients have been reported in Si, Sn, and Al systems, where nonequilibrium lithiation produces Li-rich and metal-rich domains governed by stress-composition coupling and limited Li diffusivity [75]. These gradients define dynamic reaction fronts that progressively homogenize with cycling as diffusion equilibrates, enabling strain relaxation and mitigating fracture.

The present observation of a Pt-Li gradient near the interface in Region 1 and a compositional uniformity in the underlying bulk in Region 2 is therefore consistent with these established alloying behaviors, representing kinetically distinct regimes within the same electrode: a Li-flux-limited interfacial zone and a diffusion-controlled, well-mixed bulk. The coexistence of these kinetically distinct regimes facilitates the solid-solution-type reaction mechanism observed during cycling. The Li-flux-limited interfacial zone, with its steep compositional gradients, represents the dynamic reaction front where the local rate of Li incorporation at the interface exceeds its diffusion into the alloy, leading to transient Li enrichment and compositional inhomogeneity. In contrast, the diffusion-controlled, well-mixed bulk provides a structurally stable environment where Li and Pt are homogeneously mixed, supporting reversible alloying and electrochemical stability. This partitioning between interface and bulk phases enables efficient strain accommodation and prevents

mechanical failure, critical for the sustained performance of alloying anodes when taken together with the stabilized LiF-rich SEI.

The direct observation of this behavior at high resolution has rarely been achieved, owing to Li's high mobility and beam-sensitive nature. This highlights the importance of cryo-APT as a high-resolution characterization technique for investigating alloying mechanisms in next-generation battery anodes.

IV. CONCLUSION

This work establishes a comprehensive, multilength-scale framework for resolving the coupled structural and chemical processes governing the performance of alloying anodes under realistic electrochemical conditions. By integrating *in-situ* liquid cell synchrotron hard X-ray nanoprobe XRF/XRD with cryo−STEM/EELS and cryo-APT, alloy phase evolution, interphase chemistry, and elemental distribution are directly correlated from tens of nanometeres to near-atomic resolution. This novel correlative approach enables direct tracking of lithiation-delithiation reactions and associated interfacial transformations that cannot be resolved using isolated operando liquid or cryogenic microscopy methods. This capability enables dynamic electrochemical processes occurring in liquid environments to be directly linked with preserved atomic-scale interfacial chemistry.

in-situ XRD measurements reveal a discrete phase transformation during lithiation between the Pt anode and Li electrolyte to form Li_2Pt, followed by a mechanistic shift from discrete stepwise alloying to a solid-solution type reaction during delithiation, leading to the emergence of a stable LiPt phase. These phase transformations were accompanied by the dynamic evolution of the SEI from an unstable, carbonate-rich state to a stable, LiF-dominated composition with cycling. Despite mechanical stresses and electrode redistribution during cycling revealed by XRF mapping, the persistence of the LiPt phase and LiF-rich SEI layer ensured sustained electrochemical reversibility. This work demonstrates the ability to directly track SEI components, Li metal, and alloying phase transformations using hard X-ray nanoprobes under liquid-phase electrochemical conditions.

Correlative cryogenic microscopy provides complementary nanoscale insight into these processes. Cryo-STEM and EELS mapping confirmed the presence of a dense LiF-rich SEI, while cryo-APT reveals distinct compositional regimes within the electrode: a Pt-Li compositional gradient at the interface, reflecting Li-flux-limited kinetics, and a uniform LiPt alloy deeper in the bulk, consistent with diffusion-controlled equilibrium behavior. These results provide direct experimental evidence for reaction-front-driven compositional heterogeneity and its gradual homogenization during cycling.

Collectively, these results demonstrate that long-term reversibility in alloying anodes emerges from the coupled evolution of alloy phase stability, interphase chemistry, and nanoscale mass transport. The ability to quantitatively correlate operando structural dynamics with preserved near-atomic scale interfacial chemistry represents a key methodological advance of this work. The correlative framework developed here extends beyond the Pt model system and provides a transferable strategy for interrogating complex alloy and conversion electrodes, where phase transformations, SEI instability, and mechanical degradation are tightly coupled. As such, this approach offers a powerful platform for guiding the rational design of durable, high-performance electrode materials for next-generation energy storage technologies.

ACKNOWLEDGMENTS

N. M., M. P. R., M. S. C. acknowledge funding from Engineering and Physical Sciences Research Council (EPSRC) and Shell for funding through the InFUSE Prosperity Partnership (EP/V038044/1). This work was made possible by the EPSRC Cryo-Enabled Multimicroscopy for Nanoscale Analysis in the Engineering and Physical Sciences EP/V007661/1. M. S. C. M. P., and Y. L. acknowledges funding from Royal Society Tata University Research Fellowship (URF\R1\201318) and Royal Society Enhancement Grant No. RF\ERE\210200EM1. M. S. C. acknowledges funding from ERC CoG DISCO Grant No. 101171966. SRJ thanks PhD funding from the Faraday Institution, under the Grant No. EP/S514901/1. T. S. acknowledges support from EPSRC NAME Programme Grant No. EP/V001914/1. M. P. R acknowledges support from the Armourers and Brasiers Company. We wish to acknowledge the use of the EPSRC funded Physical Sciences Data-science Service hosted by the University of Southampton and STFC under Grant No. EP/S020357/1. The authors acknowledge beamtime and data analysis support from Diamond Light Source on beamline I14 under Proposal No. MG39828. The authors used OpenAI's ChatGPT to assist with code development in this work. All outputs were verified and validated by the authors.

The authors declare that they have no known competing financial interests or personal relationships that could have appeared to influence the work reported in this paper.

DATA AVAILABILITY

Opensource Jupyter notebooks are provided as supplementary files to accompany this publication. Each notebook contains the code used for processing and analyzing the XRD and XRF datasets described in the manuscript. A brief description of the purpose and functionality of each notebook is given in the SI.

[1] H. Shin, J. M. Yoo, Y.-E. Sung, and D. Y. Chung, *Dynamic electrochemical interfaces for energy conversion and storage*, JACS Au **2**, 2222 (2022).

[2] S. J. An, J. Li, C. Daniel, D. Mohanty, S. Nagpure, and D. L. Wood III, *The state of understanding of the lithium-ion-battery graphite solid electrolyte interphase (SEI) and its relationship to formation cycling*, Carbon **105**, 52 (2016).

[3] W. Dachraoui and R. Erni, *Anode-electrolyte interface in lithium-ion batteries investigated by liquid phase transmission electron microcopy: Achievements, challenges, and future directions*, Nano Energy **143**, 111321 (2025).

[4] C. D. Quilty, D. Wu, W. Li, D. C. Bock, L. Wang, L. M. Housel, A. Abraham, K. J. Takeuchi, A. C. Marschilok, and E. S. Takeuchi, *Electron and ion transport in lithium and lithium-ion battery negative and positive composite electrodes*, Chem. Rev. **123**, 1327 (2023).

[5] G. Liang, C. Zhang, L. Yang, Y. Liu, M. Liu, X. Xiong, C. Yang, X. Lv, W. You, and K. Pei, *Probing interfacial nanostructures of electrochemical energy storage systems by in-situ transmission electron microscopy*, Nano-Micro Lett. **17**, 1 (2025).

[6] A. S. Kulathuvayal and Y. Su, *Ionic transport through the solid electrolyte interphase in lithium-ion batteries: A review from first-principles perspectives*, ACS Appl. Energy Mater. **6**, 5628 (2023).

[7] H. Adenusi, G. A. Chass, S. Passerini, K. V. Tian, and G. Chen, *Lithium batteries and the solid electrolyte interphase (SEI)—progress and outlook*, Adv. Energy Mater. **13**, 2203307 (2023).

[8] W. Dachraoui, R.-S. Kühnel, C. Battaglia, and R. Erni, *Nucleation,Growth and Dissolution of Li Metal Dendrites and the Formation of Dead Li in Li-Ion Batteries Investigated by Operando Electrochemical Liquid Cell Scanning Transmission Electron Microscopy*, Nano Energy **130**, 110086 (2024).

[9] N. Mulcahy, S. R. Jannat, G. Topore, L. Worch, J. O. Douglas, B. Gault, M. P. Ryan, and M. S. Conroy, *Degradation and SEI Evolution in Alloy Anodes Revealed by Correlative Liquid-Cell Electrochemistry and Cryogenic Microscopy.*

[10] M. J. Zachman, Z. Tu, S. Choudhury, L. A. Archer, and L. F. Kourkoutis, *Cryo-STEM mapping of solid–liquid interfaces and dendrites in lithium-metal batteries*, Nature (London) **560**, 345 (2018).

[11] J. S. Edge, S. O'Kane, R. Prosser, N. D. Kirkaldy, A. N. Patel, A. Hales, A. Ghosh, W. Ai, J. Chen, and J. Yang, *Lithium ion battery degradation: What you need to know*, Phys. Chem. Chem. Phys. **23**, 8200 (2021).

[12] P. Abellan, B. L. Mehdi, L. R. Parent, M. Gu, C. Park, W. Xu, Y. Zhang, I. Arslan, J.-G. Zhang, C.-M. Wang, J. E. Evans, and N. D. Browning, *Probing the degradation mechanisms in electrolyte solutions for Li-ion batteries by in situ transmission electron microscopy*, Nano Lett. **14**, 1293 (2014).

[13] B. L. Mehdi, J. Qian, E. Nasybulin, C. Park, D. A. Welch, R. Faller, H. Mehta, W. A. Henderson, W. Xu, and C. M. Wang, *Observation and quantification of nanoscale processes in lithium batteries by operando electrochemical (S)TEM*, Nano Lett. **15**, 2168 (2015).

[14] W. Dachraoui, R. Pauer, C. Battaglia, and R. Erni, *Operando electrochemical liquid cell scanning transmission electron microscopy investigation of the growth and evolution of the mosaic solid electrolyte interphase for lithium-ion batteries*, ACS Nano **17**, 20434 (2023).

[15] N. de Jonge, L. Houben, R. E. Dunin-Borkowski, and F. M. Ross, *Resolution and aberration correction in liquid cell transmission electron microscopy*, Nat. Rev. Mater. **4**, 61 (2019).

[16] S. Pu, C. Gong, and A. W. Robertson, *Liquid Cell Transmission Electron Microscopy and Its Applications*, R. Soc. Open Sci. **7**, 191204 (2020).

[17] N. Hodnik, G. Dehm, and K. J. Mayrhofer, *Importance and challenges of electrochemical in situ liquid cell electron microscopy for energy conversion research*, Acc. Chem. Res. **49**, 2015 (2016).

[18] G. T. van de Kerkhof, J. M. Walker, S. Agrawal, S. M. Clarke, M. H. Sk, D. J. Craske, R. Lindsay, M. Dowhyj, A. Osundare, and M. E. Schuster, *An in situ liquid environment for synchrotron hard X-ray nanoprobe microscopy*, Mater. High Temp. **40**, 371 (2023).

[19] F. Lin, Y. Liu, X. Yu, L. Cheng, A. Singer, O. G. Shpyrko, H. L. Xin, N. Tamura, C. Tian, and T.-C. Weng, *Synchrotron X-ray analytical techniques for studying materials electrochemistry in rechargeable batteries*, Chem. Rev. **117**, 13123 (2017).

[20] S.-M. Bak, Z. Shadike, R. Lin, X. Yu, and X.-Q.Yang, *Yang, In situ/operando synchrotron-based X-ray techniques for lithium-ion battery research*, NPG Asia Mater. **10**, 563 (2018).

[21] A. P. Black, A. Sorrentino, F. Fauth, I. Yousef, L. Simonelli, C. Frontera, A. Ponrouch, D. Tonti, and M. R. Palacín, *Synchrotron radiation based operando characterization of battery materials*, Chem. Sci. **14**, 1641 (2023).

[22] S. Lou, N. Sun, F. Zhang, Q. Liu, and J. Wang, *Tracking battery dynamics by operando synchrotron x-ray imaging: operation from liquid electrolytes to solid-state electrolytes*, Acc. Mater. Res. **2**, 1177 (2021).

[23] G. T. van de Kerkhof, C. Murphy, S. H. Abdulrahman, T. Poon, C. Hawkins, M. Li, A. E. Goode, J. E. Parker, and M. E. Hard Schuster, *X-ray spectromicroscopy of Ni-rich cathodes under in situ liquid heating conditions*, J. Microsc. **299**, 16 (2025).

[24] P. D. Quinn, L. Alianelli, M. Gomez-Gonzalez, D. Mahoney, F. Cacho-Nerin, A. Peach, and J. E. Parker, *The hard X-ray nanoprobe beamline at diamond light source*, Synchrotron Radiat. **28**, 1006 (2021).

[25] X. Liu, D. Wang, G. Liu, V. Srinivasan, Z. Liu, Z. Hussain, and W. Yang, *Distinct charge dynamics in battery electrodes revealed by in situ and operando soft X-ray spectroscopy*, Nat. Commun. **4**, 2568 (2013).

[26] N. Mulcahy, J. O. Douglas, S. R. Jannat, L. Worch, G. Topore, B. Gault, M. P. Ryan, and M. S. Conroy, *A workflow for correlative in situ nanochip liquid cell transmission electron microscopy and atom probe tomography enabled by cryogenic plasma focused ion beam*, Nanoscale Horiz. **10**, 3486 (2025).

[27] Y.-S. Chen, M. J. Griffith, and J. M. Cairney, *Cryo atom probe: Freezing atoms in place for 3D mapping*, Nano Today **37**, 101107 (2021).

[28] B. Gault, A. Chiaramonti, O. Cojocaru-Mirédin, P. Stender, R. Dubosq, C. Freysoldt, S. K. Makineni, T. Li, M. Moody, and J. M. Cairney, *Atom probe tomography*, Nat. Rev. Methods Primers **1**, 51 (2021).

[29] W. Huang, J. Wang, M. R. Braun, Z. Zhang, Y. Li, D. T. Boyle, P. C. McIntyre, and Y. Cui, *Dynamic structure and chemistry of the silicon solid-electrolyte interphase visualized by cryogenic electron microscopy*, Matter **1**, 1232 (2019).

[30] B. Han, Y. Zou, Z. Zhang, X. Yang, X. Shi, H. Meng, H. Wang, K. Xu, Y. Deng, and M. Gu, *Probing the Na metal solid electrolyte interphase via cryo-transmission electron microscopy*, Nat. Commun. **12**, 3066 (2021).

[31] J. E. Parker, M. Gomez-Gonzalez, Y. Van Lishout, H. Islam, D. Duran Martin, D. Ozkaya, P. D. Quinn, and M. E. Schuster, *A cell design for correlative hard X-ray nanoprobe and electron microscopy studies of catalysts under in situ conditions*, Synchrotron Radiat. **29**, 431 (2022).

[32] Y. Huang, Q. Gu, Z. Guo, W. Liu, Z. Chang, Y. Liu, F. Kang, L. Dong, and C. Xu, *Unraveling dynamical behaviors of zinc metal electrodes in aqueous electrolytes through an operando study*, Energy Storage Mater. **46**, 243 (2022).

[33] N. Williard, B. Sood, M. Osterman, and M. Pecht, *Disassembly methodology for conducting failure analysis on lithium–ion batteries*, J. Mater. Sci. Mater. Electron. **22**, 1616 (2011).

[34] R. Zhang, S. Yang, H. Li, T. Zhai, and H. Li, *Air sensitivity of electrode materials in* Li/Na *ion batteries: Issues and strategies*, InfoMat **4**, e12305 (2022).

[35] See Supplemental Material at http://link.aps.org/supplemental/10.1103/r3tc-hr17 for descriptions of the custom Python notebooks used for X-ray data processing, supplementary tables (T1–T4), supplementary figures (S1–S11), further experimental details, additional XRD/XRF datasets, cryo-FIB/SEM images, cryo-STEM EDX/EELS maps, and extended cryo-APT analysis.

[36] L. T. Stephenson, A. Szczepaniak, I. Mouton, K. A. K. Rusitzka, A. J. Breen, U. Tezins, A. Sturm, D. Vogel, Y. Chang, P. Kontis *et al.*, *The laplace project: An integrated suite for preparing and transferring atom probe samples under cryogenic and UHV conditions*, PLoS One **13**, e0209211 (2018).

[37] S. Kleindiek, A. Rummel, and K. Schock, *E-beam hardening SEM glue for fixation of small objects in the SEM*, *EMC 2008 14th European Microscopy Congress 1-5 September 2008, Aachen, Germany: Volume 1: Instrumentation and Methods* (Springer, New York, 2008), pp. 565–566.

[38] N. Mulcahy, J. O. Douglas, and M. S. Conroy, *What you made me glue: SEMGluTM enabled alternative cryogenic aample preparation process for cryogenic atom probe tomography studies*, Microsc. Microanal. **31**, ozaf063 (2025).

[39] O. M. Magnussen, J. Drnec, C. Qiu, I. Martens, J. J. Huang, R. Chattot, and A. Singer, *In situ and operando X-ray scattering methods in electrochemistry and electrocatalysis*, Chem. Rev. **124**, 629 (2024).

[40] Y. Kim, W. Choi, O.-H. Kim, H. Park, S. Yun, R. Thangavel, Y.-H. Cho, and W.-S. Yoon, *Dual lithium storage of Pt electrode: Alloying and reversible surface layer*, J. Mater. Chem. A **9**, 18377 (2021).

[41] M. Martins, D. Haering, J. G. Connell, H. Wan, K. L. Svane, B. Genorio, P. Farinazzo Bergamo Dias Martins, P. P. Lopes, B. Gould, and F. Maglia, *Role of catalytic conversions of ethylene carbonate, water, and HF in forming the solid-electrolyte interphase of Li-ion batteries*, ACS Catal. **13**, 9289 (2023).

[42] M. Yang, J. Zhang, Z. Ren, B. Wang, H. Li, and J. Cheng, Li_2CO_3/LiF*-rich solid electrolyte interface stabilized lithium metal anodes for durable* Li-CO_2 *batteries*, Energy Storage Mater. **73**, 103843 (2024).

[43] D. Cao, C. Tan, and Y. Chen, *Oxidative decomposition mechanisms of lithium carbonate on carbon substrates in lithium battery chemistries*, Nat. Commun. **13**, 4908 (2022).

[44] L. Shi, T. Qu, D. Liu, Y. Deng, B. Yang, and Y. Dai, *Process of thermal decomposition of lithium carbonate Materials Processing Fundamentals 2020* (Springer, New York, 2020), pp. 107–116.

[45] E. Feyzi, M. R. A.K., X. Li, S. Deng, J. Nanda, and K. Zaghib, *A comprehensive review of silicon anodes for high-energy lithium-ion batteries: Challenges, latest developments, and perspectives*, Next Energy **5**, 100176 (2024).

[46] B. L. Henke, E. M. Gullikson, and J. C. Davis, *X-ray interactions: Photoabsorption, scattering, transmission, and reflection at* $E = 50$–$30{,}000$ eV, $Z = 1$–92, At. Data Nucl. Data Tables **54**, 181 (1993).

[47] J. Tan, J. Matz, P. Dong, J. Shen, and M. Ye, *A growing appreciation for the role of LiF in the solid electrolyte interphase*, Adv. Energy Mater. **11**, 2100046 (2021).

[48] Z. Li, L. Wang, X. Huang, and X. He, *Unveiling the mystery of LiF within solid electrolyte interphase in lithium batteries*, Small **20**, 2305429 (2024).

[49] P. Bach, I. Valencia-Jaime, U. Rütt, O. Gutowski, A. H. Romero, and F. U. Renner, *Electrochemical lithiation cycles of gold anodes observed by in situ high-energy X-ray diffraction*, Chem. Mater. **28**, 2941 (2016).

[50] M. Pin, J. Choi, J. H. Chang, A. S. Schenk, J. Han, S. Wacławek, Y. Kim, and J. Y. Cheong, *In situ X-ray based analysis of anode materials for lithium-ion batteries: Current status and future implications*, Energy Storage Mater. **73**, 103798 (2024).

[51] S. Misra, N. Liu, J. Nelson, S. S. Hong, Y. Cui, and M. F. Toney, *In situ X-ray diffraction studies of (De) lithiation mechanism in silicon nanowire anodes*, Acs Nano **6**, 5465 (2012).

[52] W. Zhu, D. Liu, A. Paolella, C. Gagnon, V. Gariépy, A. Vijh, and K. Zaghib, *Application of operando X-ray diffraction and Raman spectroscopies in elucidating the behavior of cathode in lithium-ion batteries*, Front. Energy Res. **6**, 66 (2018).

[53] T. A. Assefa, A. F. Suzana, L. Wu, R. J. Koch, L. Li, W. Cha, R. J. Harder, E. S. Bozin, F. Wang, and I. K. Robinson, *Imaging the phase transformation in single particles of the lithium titanate anode for lithium-ion batteries*, ACS Appl. Energy Mater. **4**, 111 (2021).

[54] C. Albenga, J. A. Gott, A. Skurtveit, J. M. Warnett, F. M. Maddar, A. Y. Koposov, G. Pinzón, G. West, and I. Hasa,

Assessing the role of morphological changes as the origin of improved cycling stability of Sn-based anodes for sodium-ion batteries, J. Mater. Chem. A **13**, 30967 (2025).

[55] A. A. Topalov, S. Cherevko, A. R. Zeradjanin, J. C. Meier, I. Katsounaros, and K. J. J. Mayrhofer, *Towards a comprehensive understanding of platinum dissolution in acidic media*, Chem. Sci. **5**, 631 (2014).

[56] J. Ranninger, S. J. Wachs, J. Möller, K. J. Mayrhofer, and B. B. Berkes, *On-line monitoring of dissolution processes in nonaqueous electrolytes–a case study with platinum*, Electrochem. Comm. **114**, 106702 (2020).

[57] B. Han, Z. Zhang, Y. Zou, K. Xu, G. Xu, H. Wang, H. Meng, Y. Deng, J. Li, and M. Gu, *Poor stability of* Li_2CO_3 *in the solid electrolyte interphase of a lithium-metal anode revealed by cryo-electron microscopy*, Adv. Mater. **33**, 2100404 (2021).

[58] T. Jung, A. A. Wang, and C. W. Monroe, *Overpotential from cosolvent imbalance in battery electrolytes:* $LiPF_6$ *in EMC: EC*, ACS Omega **8**, 21133 (2023).

[59] S. Ernst, T. P. Heins, N. Schlüter, and U. Schröder, *Capturing the current-overpotential nonlinearity of lithium-ion batteries by nonlinear electrochemical impedance spectroscopy (NLEIS) in charge and discharge direction*, Front. Energy Res. **7**, 151 (2019).

[60] J. Shi, H. Gao, G. Hu, and Q. Zhang, *Confined interfacial assembly of controlled* $Li_2Ti_3O_7$ *building blocks and Si nanoparticles in Lithium-ion batteries*, Energy Storage Mater. **44**, 239 (2022).

[61] M. J. Lacey, *Influence of the electrolyte on the internal resistance of lithium−sulfur batteries studied with an intermittent current interruption method*, ChemElectroChem **4**, 1997 (2017).

[62] Y. He, Y. Cui, Z. Zhao, Y. Chen, W. Shang, and P. Tan, *Strategies for bubble removal in electrochemical systems*, Energy Rev. **2**, 100015 (2023).

[63] F. Sepahi, R. Verzicco, D. Lohse, and D. Krug, *Mass transport at gas-evolving electrodes*, J. Fluid Mech. **983**, A19 (2024).

[64] P. J. Lamas-Ardisana, G. Martínez-Paredes, L. Añorga, and H. J. Grande, *The effect of the evaporation rate on electrochemical measurements with paper-based analytical devices and its minimisation by enclosure with adhesive tape*, Electrochem. Comm. **101**, 6 (2019).

[65] F. Dai and M. Cai, *Best practices in lithium battery cell preparation and evaluation*, Commun. Mater. **3**, 64 (2022).

[66] M. Sina, R. Thorpe, S. Rangan, N. Pereira, R. A. Bartynski, G. G. Amatucci, and F. Cosandey, *Investigation of SEI layer formation in conversion iron fluoride cathodes by combined STEM/EELS and XPS*, J. Phys. Chem. C **119**, 9762 (2015).

[67] F. Wang, J. Graetz, M. S. Moreno, C. Ma, L. Wu, V. Volkov, and Y. Zhu, *Chemical distribution and bonding of lithium in intercalated graphite: Identification with optimized electron energy loss spectroscopy*, ACS Nano **5**, 1190 (2011).

[68] H. Koh, E. Detsi, and E. A. Stach, *Observation of order and disorder in solid-electrolyte interphases of lithium-metal anodes*, ACS Energy Lett. **10**, 4361 (2025).

[69] H. Li, T. Yamaguchi, S. Matsumoto, H. Hoshikawa, T. Kumagai, N. L. Okamoto, and T. Ichitsubo, *Circumventing huge volume strain in alloy anodes of lithium batteries*, Nat. Commun. **11**, 1584 (2020).

[70] Z. Wang, J. Wang, J. Ni, and L. Li, *Structurally durable bimetallic alloy anodes enabled by compositional gradients*, Adv. Sci. **9**, 2201209 (2022).

[71] W. Qi, J. G. Shapter, Q. Wu, T. Yin, G. Gao, and D. Cui, *Nanostructured anode materials for lithium-ion batteries: Principle, recent progress and future perspectives*, J. Mater. Chem. A **5**, 19521 (2017).

[72] H. S. Majdi, Z. A. Latipov, V. Borisov, N. O. Yuryevna, M. M. Kadhim, W. Suksatan, I. H. Khlewee, and E. Kianfar, *Nano and battery anode: A review*, Nanoscale Res. Lett. **16**, 177 (2021).

[73] W. Bronger, B. Nacken, and K. Ploog, *Zur synthese und struktur von* Li_2Pt *und* LiPt, J. Less Common Met. **43**, 143 (1975).

[74] J. Sangster and A. Pelton, *The Li-Pt (lithium-platinum) system*, J. Phase Equilib. **12**, 678 (1991).

[75] H. K. Seo, J. Y. Park, J. H. Chang, K. S. Dae, M.-S. Noh, S.-S. Kim, C.-Y. Kang, K. Zhao, S. Kim, and J. M. Yuk, *Strong stress-composition coupling in lithium alloy nanoparticles*, Nat. Commun. **10**, 3428 (2019).